Fracture simulation of a demountable steel-concrete bolted connector in push-out tests

Yang, Fei; Liu, Yuqing; Xin, Haohui; Veljkovic, Milan

DOI
10.1016/j.engstruct.2021.112305

Publication date
2021

Document Version
Final published version

Published in
Engineering Structures

Citation (APA)
Yang, F., Liu, Y., Xin, H., & Veljkovic, M. (2021). Fracture simulation of a demountable steel-concrete bolted connector in push-out tests. *Engineering Structures*, *239*, 1-19. Article 112305.
https://doi.org/10.1016/j.engstruct.2021.112305

Engineering Structures 239 (2021) 112305

Contents lists available at ScienceDirect

Engineering Structures

journal homepage: www.elsevier.com/locate/engstruct

Fracture simulation of a demountable steel-concrete bolted connector in push-out tests

Fei Yang [a,b], Yuqing Liu [a,*], Haohui Xin [b,c], Milan Veljkovic [b]

[a] Department of Bridge Engineering, Tongji University, Shanghai, China
[b] Department of Engineering Structures, Delft University of Technology, Delft, the Netherlands
[c] Department of Civil Engineering, Xi'an Jiaotong University, China

ARTICLE INFO

Keywords:
Bolted connector
Demountable connector
Push-out test
Damage model
Fracture criterion
Bolt shear fracture
Bolt pretension

ABSTRACT

Many bolted connectors were proposed for use in steel-concrete composite structures over the past few decades. This is because using bolted connectors could make the assembly and disassembly of steel-concrete composite structures more convenient and reusing the dismantled structural components could also improve structural sustainability. Lots of static and fatigue experimental tests on steel-concrete bolted connectors were conducted but detailed finite element simulations including fracture of bolted connectors were rarely reported. This paper presents a series of simulations of a demountable steel-concrete bolted connector in push-out tests, which was proposed and reported by the authors of this paper before. Damage models of bolt and concrete materials are incorporated in the simulations to better understand the behaviour of the bolted connector and the failure mode of the push-out tests. Direct tension tests on bolts are simulated to calibrate the stress-strain relationship of bolt material and assumed pure shear tests on bolts are modelled to validate the fracture criterion used in the simulations. Results of modelling push-out tests indicate that the friction force at the steel-concrete interface accounts for a part of shear resistance of the bolted connector in push-out tests conducted. The load-slip curves and the fracture of bolts in push-out tests can be approximately predicted by incorporating damage models of bolt and concrete materials and considering an appropriate friction coefficient. The effects of concrete damage model, clearance in bolt hole, and pretension of short bolt on the shear performance of the bolted connector are discussed at last.

1. Introduction

Bolted connections are widely used in steel structures with the advantage of easy assembly and disassembly. In the past few decades, many bolted connectors were proposed to replace the commonly used welded stud connectors in steel-concrete composite girders to realize the demountable connection between steel girder and concrete slab. The application of bolted connectors would benefit the assembly and disassembly of steel-concrete composite structures and make it possible to reuse the dismantled structural components at the end of the service life. Lots of efforts have been made to investigate the shear performance of bolted connectors through static and fatigue push-out tests and to examine the flexural behaviour of bolt-connected composite beams through static and fatigue beam tests. In previous studies, three main categories of bolted connectors were proposed and experimentally investigated.

Dai et al. [1] transformed the commonly used headed stud connectors into demountable stud connectors with a collar and a threaded portion machined at the end of the headed studs. Experimental push-out tests and numerical modelling were implemented to examine the shear behaviour of the demountable stud connector. Lam et al. [2] and Rehman et al. [3] used the demountable stud connectors forming an innovative composite floor system, in which a composite slab with metal profiled decking was connected to a steel beam using the demountable stud connectors. Full-scale composite beams connected by demountable stud connectors and welded stud connectors were tested to investigate and compare their flexural behaviours. Results showed that these two types of composite beams had very similar structural behaviours, proving the feasibility of using demountable stud connectors in composite beams. Recently, Sencu et al. [4] reported an experimental study on the performance of the demountable stud connector at elevated temperatures.

---

* Corresponding author.
E-mail address: yql@tongji.edu.cn (Y. Liu).

https://doi.org/10.1016/j.engstruct.2021.112305
Received 18 July 2020; Received in revised form 20 March 2021; Accepted 26 March 2021

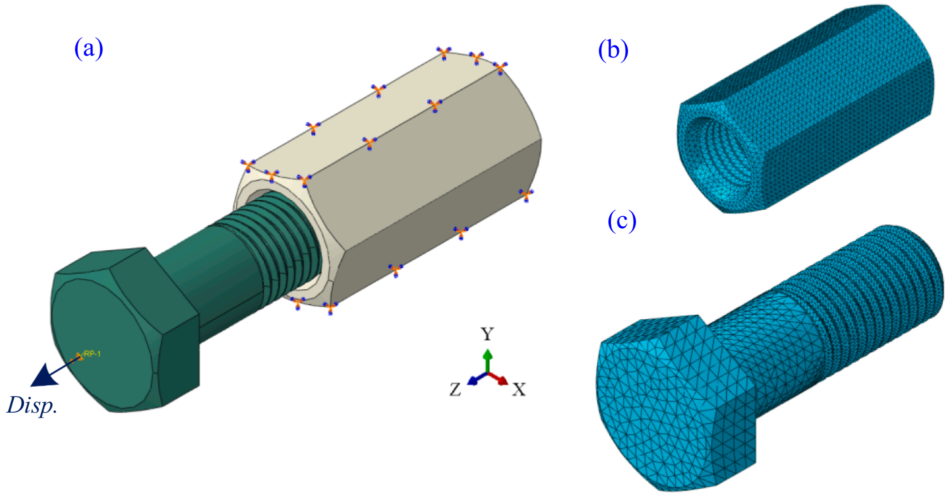

Fig. 1. FE model of M22 bolt under tension.

Kwon et al. [5,6] put forward three types bolted connectors not for the easy disassembly of composite beams but for developing composite action in existing non-composite bridges built in America before the 1970s. These three bolted connectors, including double-nut bolt, high-tension friction-grip bolt, and adhesive anchor, are all composed of the conventional bolt and nut assemblies. Four non-composite beams were strengthened using the proposed bolted connectors with a 30% shear connection ratio and then flexural load tests were conducted on the strengthened beams to investigate the contribution of the composite action to the beam bending capacity. Ghiami Azad et al. [7] conducted fatigue tests on large-scale composite beams using the post-installed adhesive anchor connectors. Results indicated that the adhesive anchor connectors had much better fatigue performance in beam tests compared to that in direct shear tests.

Yang et al. [8,9] proposed an innovative demountable steel-concrete bolted connector, consisting of a short bolt, a coupler, and a long bolt. Static push-out tests were conducted to investigate the shear performance of this “bolt-coupler” connector. Kozma et al. [10] also performed push-out tests on the “bolt-coupler” connector and some improvements, such as using epoxy resin injection bolts, were made to enhance the initial shear stiffness of the connector. Nijgh et al. [11,12] tested a tapered steel-concrete composite beam connected by resin-injected bolt-coupler connectors to investigate its disassembly and reuse abilities. Besides, requirements for oversized bolt hole in reusable composite floor systems using the resin-injected bolt-coupler connectors were studied, since the oversized holes in top flange of beams can facilitate rapid erection and easy disassembly.

It can be concluded from the performed beam tests [3,6,7,11] that arranging bolted connectors appropriately at the steel-concrete interface of composite beams can ensure the structural static and fatigue performance and make the structure disassembly feasible and convenient. In terms of push-out tests on bolted connectors, generally, only load-slip curves are recorded and failure modes are observed in experiments. The load transfer mechanism of bolted connectors is not easy to be discussed only depending on the experimental results. Detailed finite element (FE) simulations of push-out tests can help to better understand the load transfer mechanism of bolted connectors and can be used to optimize the design of bolted connectors. However, detailed FE modelling on steel-concrete bolted connectors was rarely reported before, mainly because of the complex geometry in bolt threaded portion, the uncertain property of bolt material at large deformations, and the unclear fracture behaviour of bolts under shear.

It is becoming prevailing to apply damage models in numerical analysis of steel structural behaviours. Wen and Mahmoud [13] numerically analysed the block shear failure of gusset plate in bolted connections based on a calibrated steel damage model. Feldman and Schaffrath [14,15] applied GTN damage models in the simulation of resistance and ductility of high-strength steel centre-holed plates. Recently, Xin and Veljkovic [16] calibrated an uncoupled fracture model for high-strength steels based on the uniaxial stress-strain relationship and Hosford-Coulomb fracture model. Centre-holed plates under tension and a K joint made of square hollow sections using S700 and S960 were simulated through calibrating their uniaxial stress-strain relationships and fracture models. Regarding the fracture of structural bolts, Li et al. [17,18] experimentally and numerically investigated the structural behaviours of high-strength structural bolts Grade 10.9 and 12.9 under various loading combinations. Fracture properties of the structural bolts were simulated through calibrating steel damage models in the numerical analysis. Song et al. [19,20] reported a comprehensive study on the behaviour of stainless bolts under combined tension and shear. Fracture of the stainless bolts under combined tension and shear was simulated using a calibrated steel damage model. Grimsmo et al. [21] and Yang et al. [22] successfully modelled the tensile fracture and thread stripping failure of M16 bolt and nut assemblies based on calibrated steel damage models. Therefore, in the numerical analysis of steel-concrete bolted connectors, the shear fracture of bolts could also be simulated through considering suitable steel damage model, which is beneficial for better understanding the load transfer mechanism and shear performance of the steel-concrete bolted connector investigated.

This paper presents a series of FE simulations of a demountable steel-concrete bolted connector in push-out tests, which have been published by the authors of this paper in [8]. Damage models for bolt and concrete materials are incorporated in FE simulations to better understand the behaviour of bolted connectors and the failure mode of push-out tests. Direct tension tests on bolts are simulated to verify the constitutive relationship of bolt material and assumed pure shear tests on bolts are modelled to validate the fracture criterion used. The effects of friction coefficient, concrete plastic damage model, clearance in bolt holes, and bolt pretension on the shear performance of the “bolt-coupler” connector are discussed to gain better insights into this bolted connector.

2. Modelling of tensile tests

2.1. Geometry of tensile test specimens

In the experimental program of testing the bolt-coupler connectors by the authors of this paper [8], tensile resistances of four groups of bolts were tested including grade 8.8 M18, M22, M27 bolts and grade 10.9 M22 bolts. The nominal ultimate strength for grade 8.8 and 10.9 bolts is

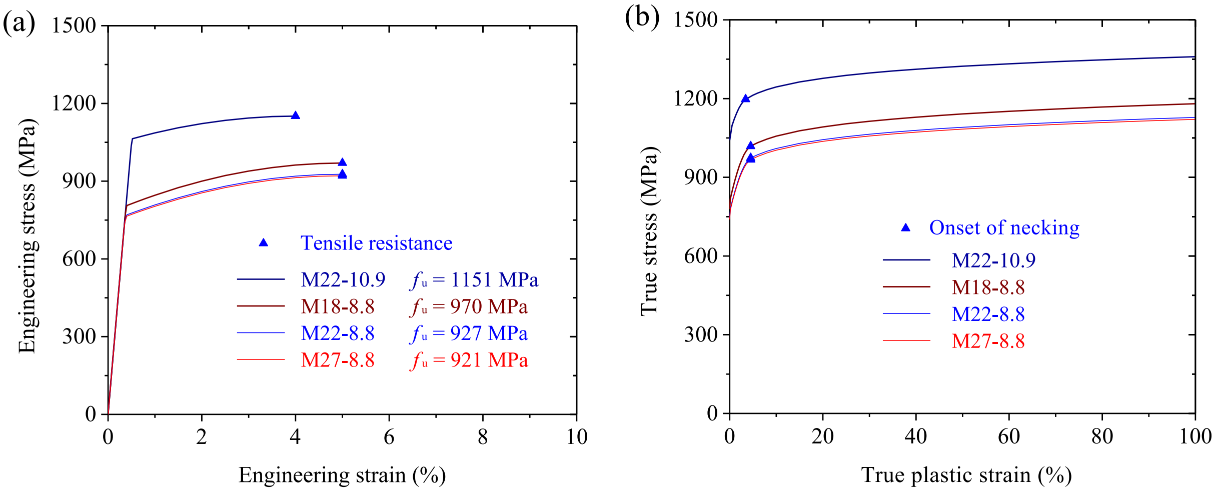

Fig. 2. Engineering and true stress-strain curves of bolts.

800 and 1000 MPa, respectively, whereas the nominal ratio of yield strength f_y to ultimate strength f_u is 0.8 and 0.9 for grade 8.8 and 10.9 bolts, respectively. Before the fracture simulation of push-out tests on the bolted connectors, bolt material properties are firstly checked through simulation of the bolt tensile tests. Fig. 1 shows the FE model of M22 bolt under tensile loading. There are two parts in the tensile assembly consisting of a bolt and a coupler. The coupler is constrained through fixing the top and bottom external surfaces, and a Z-directional displacement is applied on the bolt head, see Fig. 1a.

The measured bolt diameters are a little less than the nominal diameters, such as the diameter of M22 bolt is 21.8 mm, which is slightly less than the nominal 22.0 mm. In the simulation of the bolt assemblies, nominal dimensions of bolts and couplers are used to simplify the modelling. Therefore, the tensile stress area A_s for M18, M22, and M27 bolts is equal to 192, 303, and 459 mm^2 according to EN ISO 898 [23]. In terms of modelling the geometry of bolt assemblies, dimensions specified in [24,25] are used and more detailed descriptions relating to model the bolt assemblies have been reported in [22]. The mesh size for the coupler is 1.5 mm, while the mesh size in the threaded and unthreaded portions of the bolt is 1.0 and 3.0 mm, respectively, see Fig. 1b and 1c. The FE simulation of the bolt assemblies under tension and shear is completed using the explicit solver in ABAQUS [26]. A 10-node modified quadratic tetrahedron element C3D10M is used to mesh the bolt and a 4-node linear tetrahedron element C3D4 is used to mesh the coupler, since the main concern is the bolt behaviour and using the quadratic element can generate more accurate results.

2.2. Material behaviours

To simulate the bolt behaviour under tensile loading, full-range true stress-strain constitutive relationship of bolt material is essential in the numerical analysis. However, only ultimate tensile resistances were measured in the bolt tensile tests instead of the complete load-elongation curve [8]. According to the experimental results on bolt material reported in [21,27–29], it can be concluded that the engineering stress-strain relationship of bolt material in the plastic stage approximates a parabola, and the vertex of the parabola corresponds to the ultimate strength of bolt material. Therefore, it is assumed here that the pre-necking engineering stress-strain curve for bolts has a linear-elastic and parabolic-plastic stress-strain relationship, as shown in Fig. 2a. For grade 8.8 bolts, when the engineering strain equals to 0.05, the engineering stress gets to the ultimate strength; while for grade 10.9 bolts, the engineering strain corresponding to ultimate strength is 0.04, less than that for grade 8.8 bolts due to the less ductility [21,27]. The nominal ratios f_y/f_u equal to 0.8 and 0.9 are used here to determine the yield strength of grade 8.8 and 10.9 bolts, respectively. Based on the ultimate and yield strengths, and their respective strains, the parabola describing the pre-necking plastic stress-strain relationship of bolt material can be determined, see Fig. 2a. Accordingly, the only unknown parameter is the bolt ultimate strength, and it can be estimated using the trial-and-error method by comparing the numerical tensile resistance to the experimental value for each bolt.

Full-range true stress-strain curves for high-strength steels have been investigated in [30,31]. The pre-necking true stress-strain can be obtained by converting equations between engineering stress-strain and true stress-strain, as shown in Eqs. (1.1) and (1.2). σ_e and ε_e denote the engineering stress and strain, which can be obtained from the coupon tensile tests. σ_t and ε_t denote the true stress and strain, which should be input in the numerical analysis.

$$\sigma_t = \sigma_e(1 + \varepsilon_e) \tag{1.1}$$

$$\varepsilon_t = ln(1 + \varepsilon_e) \tag{1.2}$$

The post-necking true stress-strain diagram for high-strength steels including bolts can be approximately described using combined linear and power stress-strain law [31]. According to the recent investigation on bolts under tensile loading [22], it indicates that the post-necking true stress-strain diagram for bolts can be described using the power stress-strain law, as shown in Eq. (2).

$$\sigma_t = K\varepsilon_t^n \tag{2}$$

where, $K = \sigma_{t,u}/n^n$, $n = \varepsilon_{t,u}$. $\sigma_{t,u}$ and $\varepsilon_{t,u}$ denote the true stress and true strain at the onset of necking, respectively. Fig. 2b shows the full-range true stress vs. plastic strain curves for each bolt with a power law post-necking stress-strain relationship. The post-necking true stresses for each bolt have a slightly growing trend as the increase of plastic strain getting to as large as 1.0.

In the numerical analysis using the explicit solver in ABAQUS [26], general contact is selected to model the contact property between bolt and nut threads. The normal behaviour of the general contact is modelled using “hard” contact, while the tangential behaviour is modelled using “penalty” friction formulation with “friction coefficient” equal to 0.2. Using the “hard” contact property for the normal behaviour of surfaces can minimize the surface penetration at the constraint locations and not allow the transfer of tensile stress across the interface. When surfaces are in contact, any contact pressure can be transmitted between them, and the surfaces separate if the contact pressure reduces to zero. The tangential slip at the surface interfaces would always be zero before the shear stress at the surface interfaces get to the critical shear stress, which is equal to the “friction coefficient” times the contact

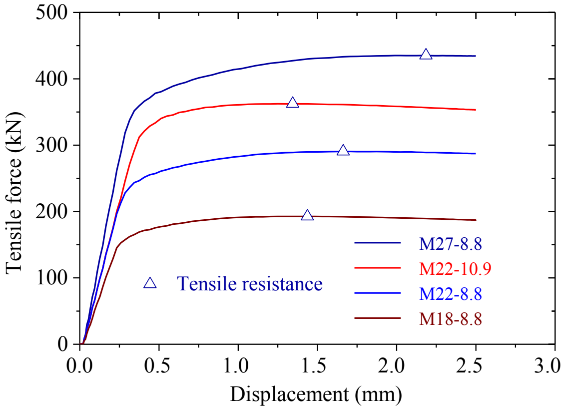

Fig. 3. Load-displacement curves of bolts under tension.

Table 1
Experimental and FEA results of tensile tests on bolts.

Bolt	Disp. (mm)	Tensile resistance (kN)	
		Experiment [8]	FEA
M18-8.8	1.44	192.5	192.7
M22-8.8	1.66	290.0	290.5
M22-10.9	1.34	360.0	362.4
M27-8.8	2.19	436.0	435.2

pressure at the interfaces. The target time increment is set to 0.002 s and the duration of the tensile loading step is 200 s. Mises criterion is adopted to describe the yield surfaces with the associated plastic flow.

After lots of calculations, it is found that the tension resistance of a bolt can be predicted using Eq. (3).

$$F_t = 0.97 f_{ub} A_s \tag{3}$$

where, F_t is the bolt tension resistance, f_{ub} is the ultimate strength of bolt material, A_s stands for the tensile stress area of each bolt, which is specified in EN ISO 898-1 [23]. In EN 1993-1-8 [32], the design tension resistance of a bolt $F_{t,Rd}$ is determined by Eq. (4).

$$F_{t,Rd} = \frac{0.9 f_{ub} A_s}{\gamma_{M_2}} \tag{4}$$

where, γ_{M_2} is a partial factor equal to 1.25. It can be concluded that the tension resistance of a bolt is slightly conservatively considered by Eq. (4) in [32], as a smaller factor 0.9 is used compared to 0.97 proposed in Eq. (3).

2.3. FEA results of tensile test modelling

According to Eq. (3), the ultimate strength f_{ub} of each bolt analysed can be obtained, as shown in Fig. 2a. The true stress-strain curves of each bolt in Fig. 2b are based on the engineering stress-strain shown in Fig. 2a and the prediction of post-necking stress-strain by Eq. (2). Fig. 3 shows the load-displacement curves of each bolt under tension. The initial tensile stiffness and the deformation capacity are slightly growing with the increase of bolt diameter for grade 8.8 bolts. Grade 10.9 M22 bolt has a smaller deformation capacity compared to grade 8.8 M22 bolt since a smaller engineering strain corresponding to ultimate strength is considered in the analysis. Here, the deformation capacity of bolts refers to the tensile displacement at the ultimate tensile force. Table 1 lists the experimental and FEA results of the tensile tests on each bolt. The FEA results agree well with the experimental results. The tensile strength of each bolt, determined by using Eq. (4), is proved to be accurate enough for modelling the tensile behaviour of bolts.

Fig. 4 shows the contour plots of equivalent plastic strain (PEEQ) and Mises stress of M22-8.8 bolt at its maximum tensile load. The PEEQ concentrates in the bolt threaded portion and most part of the bolt unthreaded portion is still in the elastic stage at the maximum tensile load. The maximum PEEQ locates in the core of the threaded portion and its value is as large as 0.1, about two times the necking true strain. The maximum Mises stress occurs in the core of the threaded portion and its value is around 1100 MPa. A slight necking in the threaded portion can be observed in Fig. 4, and the same phenomenon has been reported in the experimental tests [8].

3. Modelling of shear tests

3.1. Geometry of shear test specimens

Due to the strain localization effect in tensile tests, only considering the true stress-strain relationship of bolt material can generate the bolt tensile resistance in the numerical analysis, as shown in Fig. 3. For the simulation of bolts under shear, the damage model should also be considered to obtain the shear resistance, otherwise the numerical results would overestimate the bolt shear resistance. Although no pure shear tests were performed on bolts in the authors' previous tests [8], assumed shear tests on bolts are modelled to check the pure shear resistance of each bolt and to calibrate the relevant parameter in the fracture criterion used.

Fig. 5 shows the FE model and mesh of the pure shear test on M22 bolts. There are three parts, a bolt, a coupler, and a steel plate, in the pure shear test model. The width, height, and thickness of the steel plate is 80, 100, and 30 mm, respectively. The plate thickness is same as the plate used in push-out tests, and the thicker dimension is to avoid the plate bearing failure mode and to ensure a shear failure of bolts. The coupler is fully constrained at its exterior surfaces. A Z-directional constraint is imposed on the right surface of the plate, which would ensure the plate keeps vertical and avoid the occurrence of friction force between plate and coupler in the loading process, see Fig. 5a. A Y-directional displacement is applied on the top of the plate and the corresponding loading force can be considered equal to the bolt shear force. Same as in the tensile test modelling, general contact is selected to model the surface contact property. Element C3D8R is used to mesh the plate and only elastic properties are considered for the plate with Young's modulus and Poisson's ratio equal to 210 GPa and 0.3, respectively. Meshes for bolt and coupler are the same as in the modelling of tensile tests. Material properties of the coupler are taken the same as bolt material properties, which has been calibrated in the tensile test modelling, shown in Fig. 2b.

3.2. Fracture criterion

Lots of damage models have been proposed to explain the fracture of metal material in the past few decades [33,34]. Using reasonable damage models in the simulation of bolt assemblies makes it possible to analyse the fracture behaviour of bolts under different loadings [17–22]. As the shear fracture of bolts is the major concern in this study, an appropriate damage model which could predict the shear fracture of metal material is adopted in the analysis. Bao and Wierzbicki [35,36] conducted a series of tests including compression tests, shear tests, and tension tests on aluminium alloy. It is concluded that for negative stress triaxiality, the fracture is governed by shear mode. For larger stress triaxiality, void growth is the dominant failure mode. While at stress triaxiality between the above two regimes, the fracture develops as a combination of shear and void growth modes. The fracture criterion proposed by Bao and Wierzbicki is denoted as the BW criterion, which is a function of fracture equivalent plastic strain (PEEQ) to stress triaxiality η as expressed in Eq. (5).

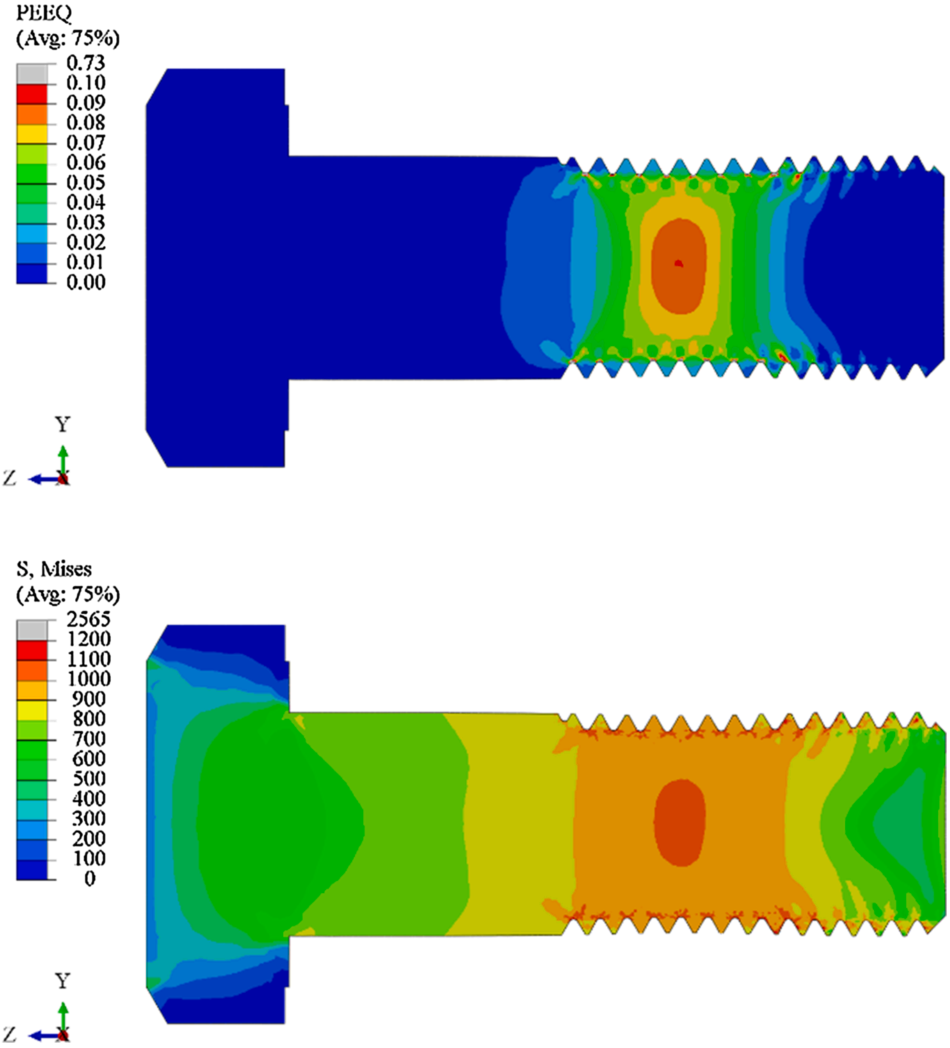

Fig. 4. Contour plots of PEEQ and Mises stress for M22-8.8 bolt at maximum load.

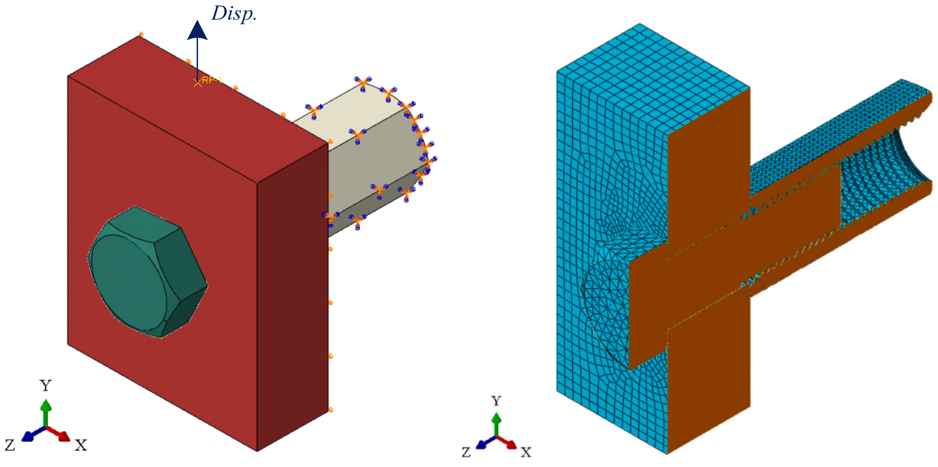

(a) FE pure shear model

(b) Mesh of the FE model

Fig. 5. FE model of M22 bolt under pure shear.

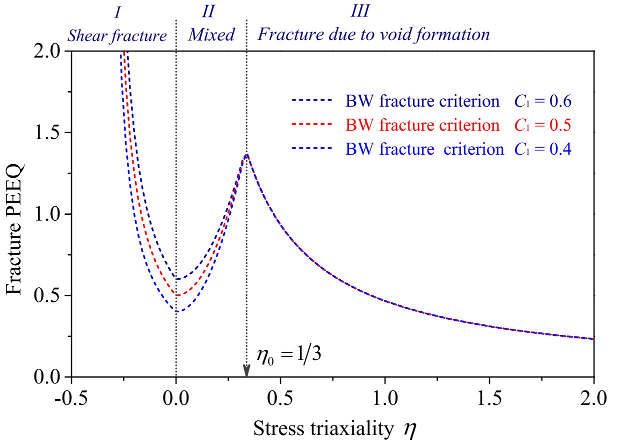

Fig. 6. Dependence of fracture PEEQ on stress triaxiality η in the BW criterion.

$$\bar{\varepsilon}_f(\eta) = \begin{cases} \infty, & \eta < -1/3; \\ \dfrac{C_1}{3\eta + 1}, & -1/3 \leqslant \eta < 0; \\ (C_2 - C_1)(\eta/\eta_0)^2 + C_1, & 0 \leqslant \eta < \eta_0; \\ \dfrac{C_2}{\eta/\eta_0}, & \eta_0 \leqslant \eta. \end{cases} \qquad (5)$$

In Eq. (5), C_1 and C_2 are two material constants governing the shear fracture and tensile fracture, which can be calibrated based on pure shear test and uniaxial tensile test, respectively.

Fig. 6 illustrates the dependence of fracture PEEQ on stress triaxiality η in the BW criterion. η_0 can be taken as 1/3 corresponding to the stress triaxiality under pure axial tension, as the fracture PEEQ at the pure tension state has the maximum value. Two constants C_1 and C_2 will determine the fracture PEEQ at each stress triaxiality. Although the BW criterion is put forward based on the tests on aluminium alloy, this criterion could also be used to simulate the fracture of steel material through calibrating the material constants C_1 and C_2 [17,18,22]. In the following section, parameter C_1 equal to 0.4, 0.5 and 0.6 will be adopted to simulate the shear fracture of bolts, while parameter C_2 is set to 1.4 according to the fracture simulation of bolts under tensile loading [22].

3.3. FEA results of shear test modelling

ABAQUS [26] offers the capability for modelling progressive damage and fracture failure of steels. This requires the definition of damage

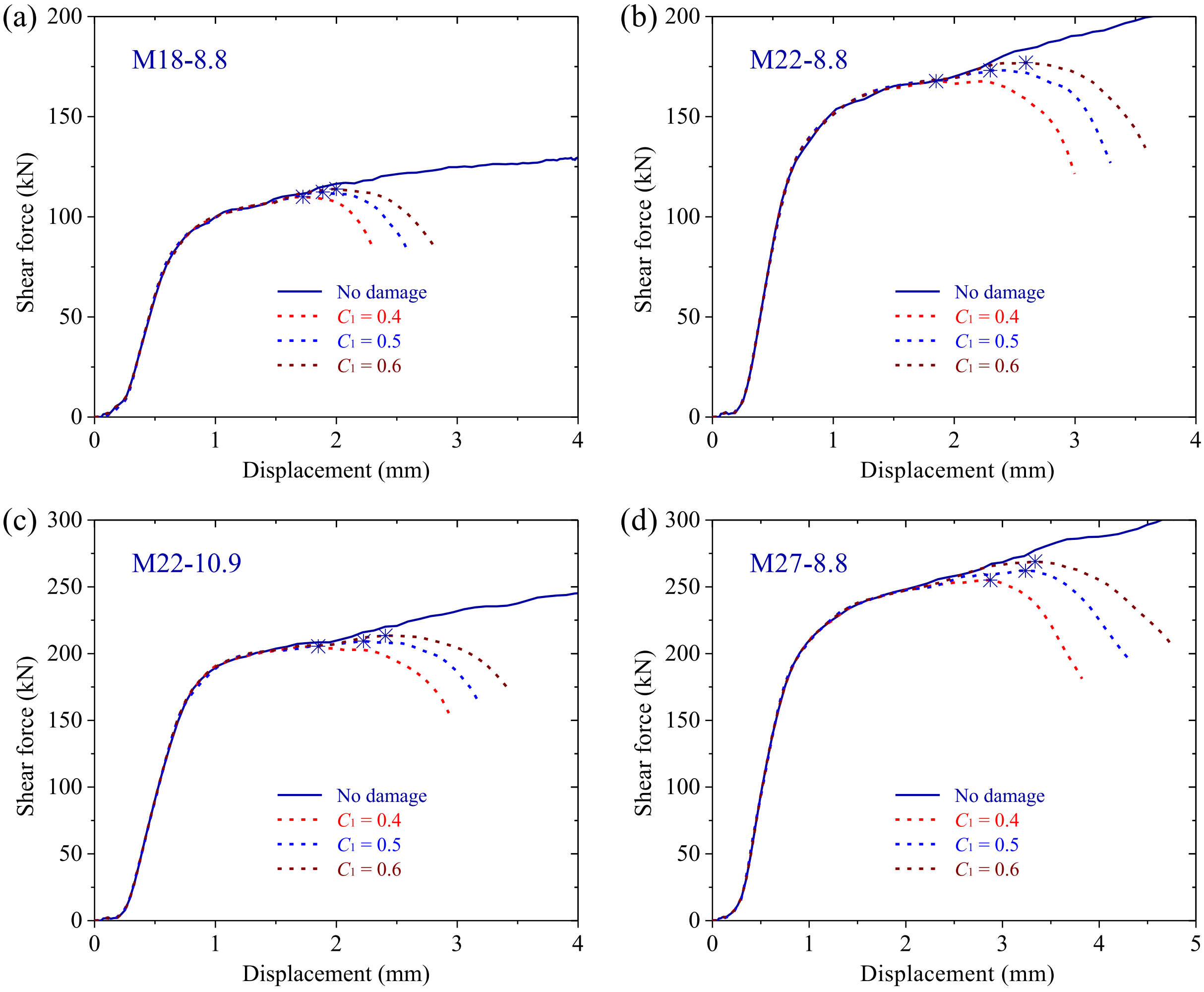

Fig. 7. Load-displacement curves of bolts under pure shear.

Table 2
FEA results of shear tests on bolts.

Bolt	Fracture parameter	Slip (mm)	Shear resistance (1) (kN)	Tensile resistance (2) (kN)	Ratio (1)/(2)
M18-8.8	$C_1 = 0.4$	1.72	110.0	192.7	0.57
	$C_1 = 0.5$	1.89	112.4		0.58
	$C_1 = 0.6$	2.00	113.9		0.59
M22-8.8	$C_1 = 0.4$	1.85	167.8	290.5	0.58
	$C_1 = 0.5$	2.30	173.1		0.60
	$C_1 = 0.6$	2.59	177.0		0.61
M22-10.9	$C_1 = 0.4$	1.85	205.5	362.4	0.57
	$C_1 = 0.5$	2.22	209.4		0.58
	$C_1 = 0.6$	2.41	213.5		0.59
M27-8.8	$C_1 = 0.4$	2.87	255.1	435.2	0.59
	$C_1 = 0.5$	3.24	262.1		0.60
	$C_1 = 0.6$	3.34	269.0		0.62

initiation criterion and damage evolution law appropriately. Only the final fracture modes of bolts are concerned in this study. Therefore, the BW criterion are taken as the damage initiation criterion. The damage evolution law is defined by the displacement type with a very small displacement at failure, such as 0.01, to achieve the sudden fracture shortly after the damage initiation. The damage initiation will occur when the condition expressed by Eq. (6) is satisfied.

$$\omega_f = \int \frac{d\bar{\varepsilon}^{pl}}{\bar{\varepsilon}_f(\eta)} = 1 \tag{6}$$

where ω_f denotes the damage index, $\bar{\varepsilon}^{pl}$ is the equivalent plastic strain (PEEQ), and $\bar{\varepsilon}_f(\eta)$ is the fracture PEEQ as expressed by Eq. (5).

Based on the true stress-strain relationship and the BW criterion, the assumed pure shear tests on grade 8.8 M18, M22, M27 and grade 10.9 M22 bolts are simulated. Fig. 7 shows the final load-displacement curves for each pure shear test. If the fracture criterion of Eq. (5) is not considered in the calculations, the shear force will continuously increase with the growth of the pull-out displacement. This can be explained by the fact that, as shown in Fig. 2b, the true stress of bolts still has a slightly increasing trend at large strain exceeding 0.5. In the bolt tensile tests, tensile necking would occur due to strain localization effect, causing that the tensile force reaches the tensile resistance before the tensile fracture of bolts, as shown in Figs. 3 and 4. Unlike the bolt tensile test, there is no “shear necking” phenomenon occurring in the bolt shear region in the bolt shear test, which will be discussed in the following section. Therefore, considering the fracture criterion is essential to obtain the bolt shear resistance in the numerical analysis. As shown in Fig. 7, with the increase of the value for parameter C_1 in the BW criterion, the deformation capacity and shear resistance of each bolt would get larger in the calculations. The effect of parameter C_1 on the deformation capacity is more significant than that on the bolt shear resistance.

Regarding the shear resistance of bolts, Renner and Lange [37] experimentally investigated the ultimate capacity of bolts under combined tension and shear. For grade 8.8 and 10.9 bolts, experimental results indicate that the shear resistance of bolts approximates 0.6 times of the tensile resistance. Li et al. [17,18] recently also reported the same ratio of shear resistance to tensile resistance for bolts based on experimental tests. These experimental results verify the accuracy of the equation in EN 1993-1-8 [25], in which the shear resistance of bolts grade 8.8 and 10.9 is specified as 0.6 times of the tensile resistance. Table 2 lists the FEA results of modelling shear tests on bolts with parameter C_1 equal to 0.4, 0.5 and 0.6 in the BW criterion. The shear resistance of each bolt is compared to their tensile resistance. The ratio of shear resistance to tensile resistance is in the range of 0.57 to 0.62. Using a bigger value for parameter C_1 in the BW criterion will lead to a slightly larger resistance ratio of shear to tension. This suggests that using the BW criterion with C_1 in the range of 0.4 to 0.6 could estimate the bolt shear resistance reasonably well. In the following analysis of push-out tests, parameter C_1 in the BW criterion is taken as 0.5 to simulate the bolt shear fracture.

Fig. 8 shows the contour plots of damage index, PEEQ, and Mises stress for M22 bolt grade 8.8 at its maximum load with parameter $C_1 = 0.5$ in the BW criterion. The bolt deformation at its maximum load can also be seen in Fig. 8 and the deformation scale is equal to 1.0. The plane shown in Fig. 8 is the vertical plane pass through the bolt axis. From the bolt deformation at its maximum load, it can be seen that the bolt cross-

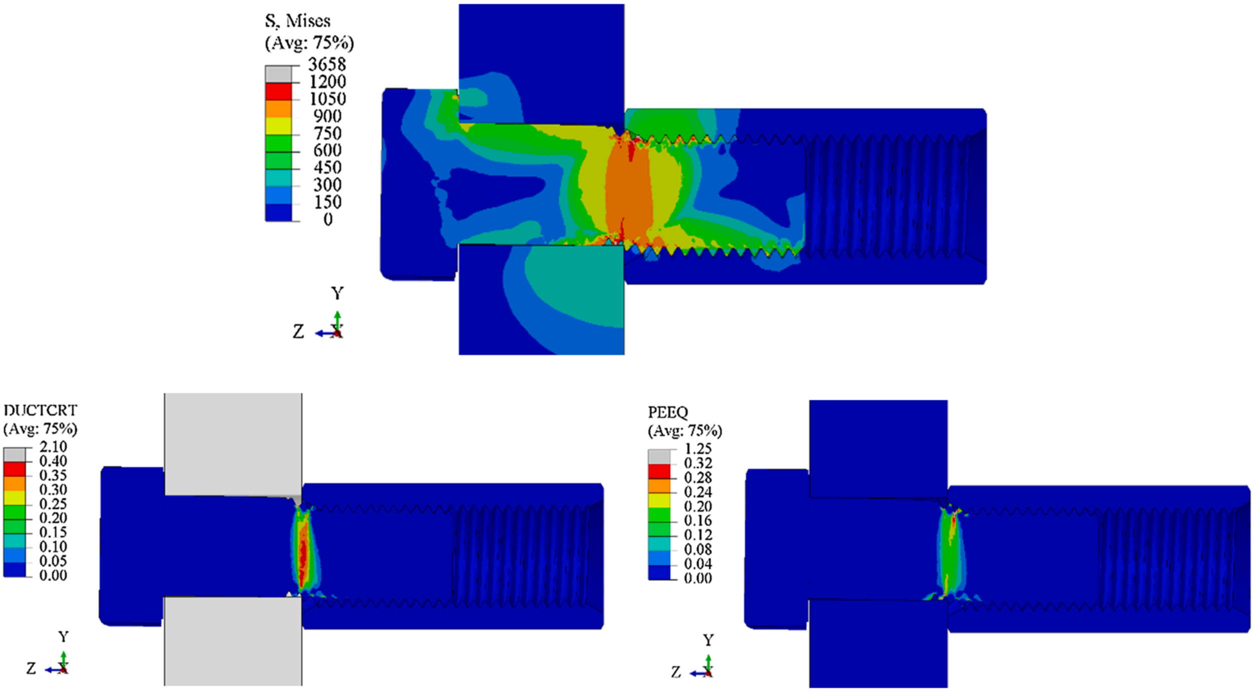

Fig. 8. Contour plots of Mises stress, damage index, PEEQ for M22-8.8 bolt at maximum load.

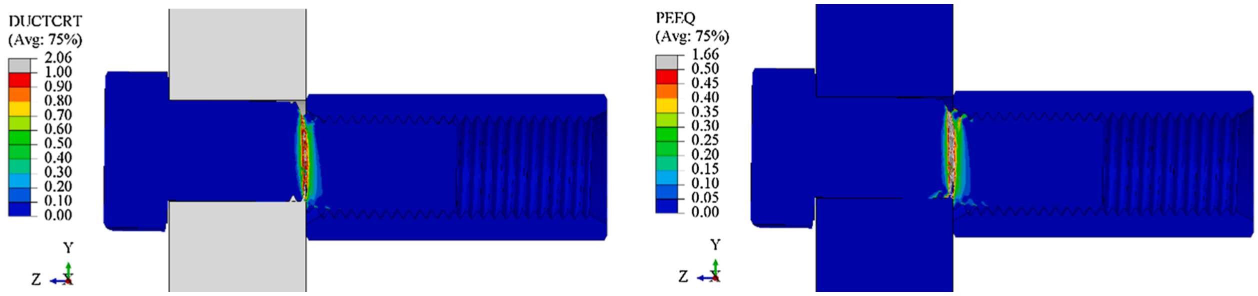

Fig. 9. Contour plots of damage index and PEEQ for M22-8.8 bolt after fracture.

(a) Front view

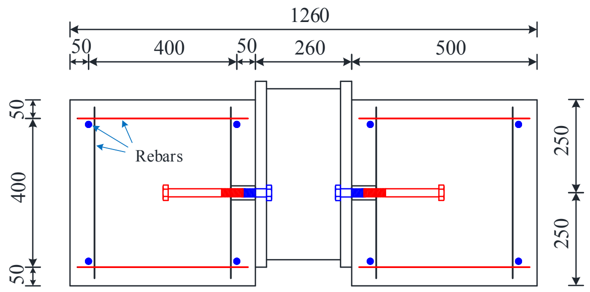

(b) Top view

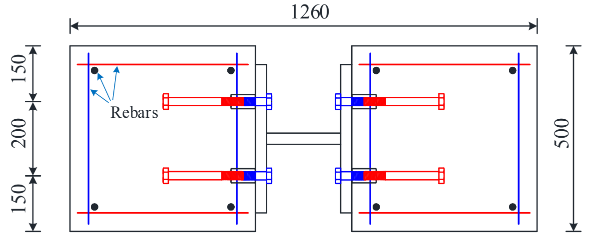

Fig. 10. Configurations and dimensions of push-out specimens (Unit: mm).

section near the shear plane has not been reduced apparently. Therefore, it is concluded that the only considering the bolt true stress-strain constitutive relationship would not obtain the bolt shear resistance, and it is the damage evolution near the shear plane causes the shear force deceasing in the bolt pure shear tests. The maximum damage index DUCTCRT in the core region of the shear plane is around 0.4. When the damage index exceeds this value, the shear resistance will decrease due to the fracture of some small regions around the threaded portion. The maximum PEEQ in the bolt shear plane is about 0.32 locating near the top engagement region of the shear plane, and the PEEQ for most part of the shear plane is around 0.2. The maximum Mises stress in the shear plane occurs in the threaded portion of the shear plane, with the maximum value around 1200 MPa.

Fig. 9 shows the contour plots of damage index and PEEQ for M22 bolt grade 8.8 when fracture occurs. The bolt fracture is triggered when the damage index DUCTCRT in the shear plane gets to 1.0, namely the satisfaction of Eq. (6). At this moment the PEEQ in major region of the shear plane is equal to 0.5, which is governed by parameter C_1 in the BW criterion.

4. Modelling of push-out tests

4.1. Geometry of push-out specimens

Push-out tests on the “bolt-coupler” steel-concrete connectors reported in [8] by the authors of this paper are numerically investigated. Fig. 10 shows the configurations and dimensions of the push-out specimens for investigating the shear performance of the proposed “bolt-coupler” connectors. Four groups of push-out tests on “bolt-coupler” connectors were conducted including grade 8.8 M18, M22, M27 bolts and grade 10.9 M22 specimens. In each push-out specimen, there are four “bolt-coupler” connectors to connect the two concrete blocks to the central steel component with H cross-section, see Fig. 10. The concrete block is a cube with an edge of 50 cm and the connectors are embedded into the central region of the concrete blocks. The rebars embedded in the concrete block has a diameter of 16 mm and a length of 46 cm. The distance of the rebar axis to the nearest concrete surface is 50 mm. The yield strength of the rebar is near 355 MPa. In the tests, the steel component was pushed out and the relative slips between concrete and steel component near the bolts were measured.

In the FE simulation of push-out tests, only a quarter of the push-out specimen with one “bolt-coupler” connector is modelled to improve the computational efficiency, see Fig. 11. There are in total seven parts in the model, including steel plate, concrete block, base plate, rebar mesh, short bolt, coupler, and long bolt. Four groups of push-out specimens are modelled, M18-8.8, M22-8.8, M22-10.9, and M27-8.8. The symmetrical boundary conditions about X- and Z-axes are applied on the surface 1 and surface 2, respectively, as shown in Fig. 11a. For surface 1, which is the middle plane parallel to YZ plane passing through the steel component and concrete block, its X-directional displacement and rotation about Y- and Z-axes are set to zero. Whereas for surface 2, which is a plane parallel to the XY plane passing through the centre of the steel web, its Z-directional displacement and rotation about X- and Y-axes are set to zero. A rigid plate is used to model the base plate, and all freedoms of its underside surface are constrained. A negative Y-directional displacement is applied on the top surface of the steel plate to apply the push-out action.

Fig. 11 also shows the element type for each part. An 8-node linear brick with reduced integration element C3D8R, having just a single integration point located at the element’s centroid, is used in steel plate and concrete block. A rigid element R3D4 is used in base plate. The same mesh and element are used for short bolts and couplers as in the pure shear test modelling. A linear tetrahedral element C3D4 is used for long bolt with a coarse mesh to reduce the computational cost.

4.2. Concrete uniaxial behaviours

Plastic damage model is used to simulate concrete behaviour in push-out tests. Alfarah et al. [38] recently proposed a new methodology for calculating damage variables in concrete plastic damage model, based on which numerical results are insensitive of mesh size since a strategy aiming to avoid mesh-dependency is incorporated in the methodology. The input parameters are concrete compressive strength and mesh size, which make it very practical in modelling concrete behaviour in the push-out tests of this paper. The uniaxial stress-strain behaviour, plastic model, and damage variables of concrete are briefly introduced as follows.

In terms of the concrete constitutive laws proposed in [38], both

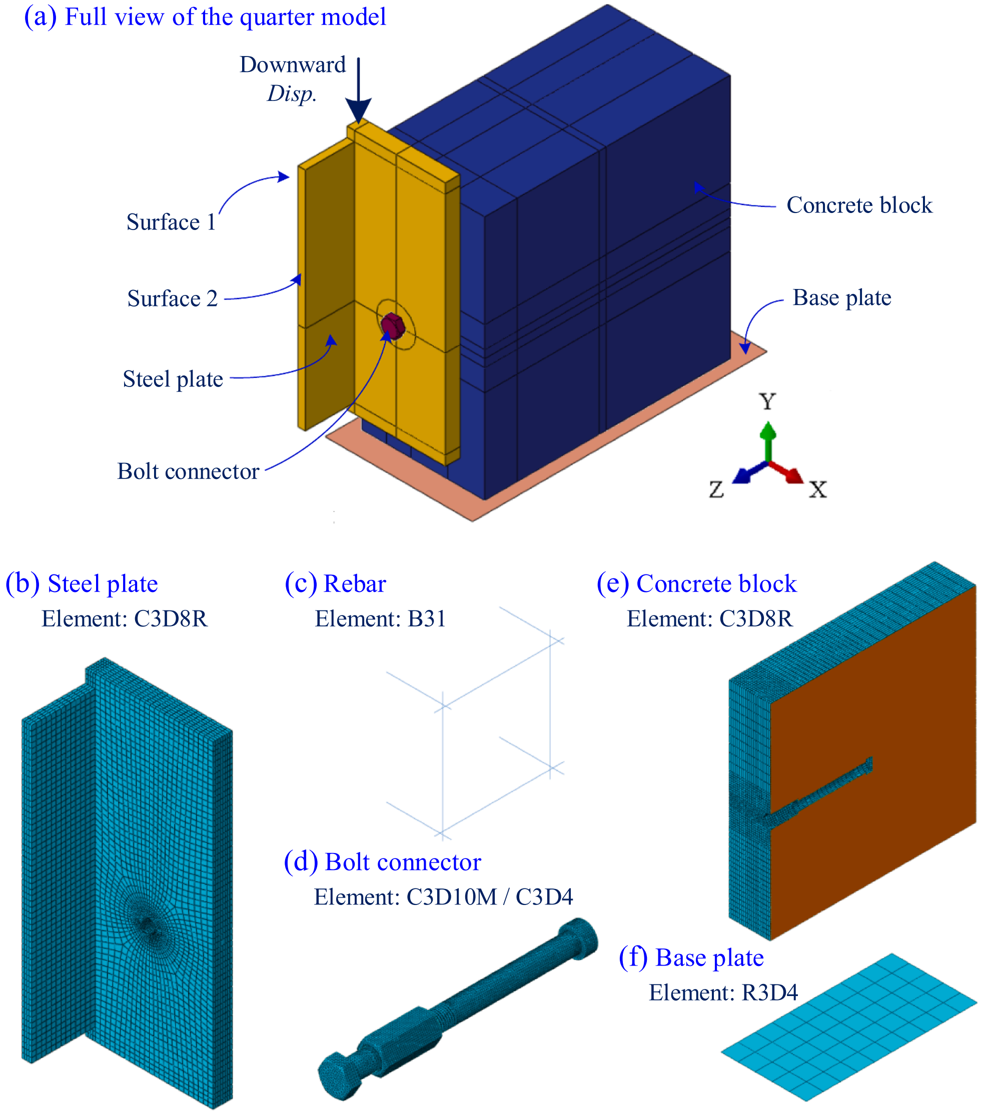

Fig. 11. FE model of push-out tests.

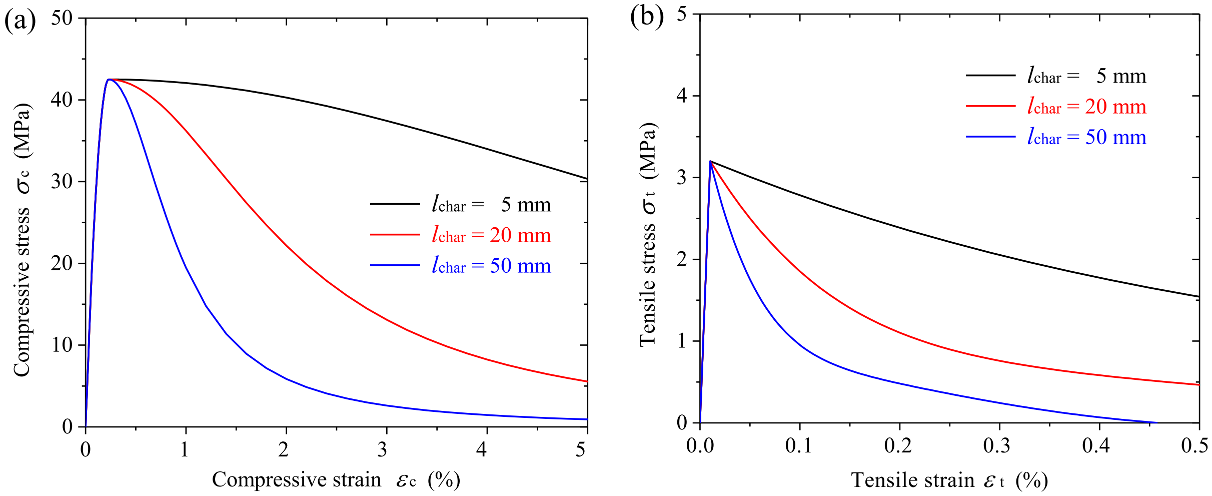

Fig. 12. Mesh-dependent stress-strain curves for concrete under compression and tension.

Table 3
Concrete properties in the uniaxial stress-strain behaviour (Concrete grade C35).

Parameter	Value
$f_{cm,cube}$	52.4 MPa
f_{cm}	42.4 MPa
ε_{cm}	0.0023
$f_{ck} = f_{cm} - \Delta f$	34.5 MPa
$f_{tm} = 0.3(f_{ck})^{2/3}$	3.2 MPa
$E_{ci} = 10000(f_{cm})^{1/3}$	34800 MPa
$E_c = (0.8 + 0.2f_{cm}/88)E_{ci}$	31200 MPa
$G_F = 0.073(f_{cm})^{0.18}$	0.143 N/mm
$G_{ch} = (f_{cm}/f_{tm})^2 G_F$	25.3 N/mm
$w_c = 5G_F/f_{tm}$	0.224 mm

compressive and tensile softening branches in the uniaxial stress-strain curves depend on mesh size, as shown in Fig. 12. There are three parts in the compressive stress-strain curve, the linear ascending part reaching $f_{c0} = 0.4f_{cm}$, the quadratic ascending part from f_{c0} to f_{cm}, and the descending part, corresponding to Eqs. (7.1), (7.2), and (7.3), respectively. f_{c0} and f_{cm} represents the limit of linear compressive stress and mean value of concrete cylinder compressive strength, respectively.

$$\sigma_{c(1)} = E_c \varepsilon_c \tag{7.1}$$

$$\sigma_{c(2)} = \frac{E_{ci}\frac{\varepsilon_c}{f_{cm}} - \left(\frac{\varepsilon_c}{f_{cm}}\right)^2}{1 + \left(E_{ci}\frac{\varepsilon_c}{f_{cm}} - 2\right)\frac{\varepsilon_c}{\varepsilon_{cm}}} f_{cm} \tag{7.2}$$

$$\sigma_{c(3)} = \left(\frac{2 + \gamma_c f_{cm}\varepsilon_{cm}}{2f_{cm}} - \gamma_c \varepsilon_c + \frac{\varepsilon_c^2 \gamma_c}{2\varepsilon_{cm}}\right)^{-1} \tag{7.3}$$

$$\gamma_c = \frac{\pi^2 f_{cm}\varepsilon_{cm}}{2\left[\frac{G_{ch}}{l_{char}} - 0.5f_{cm}\left(\varepsilon_{cm}(1-b) + b\frac{f_{cm}}{E_c}\right)\right]^2} \tag{7.4}$$

The ascending parts described by Eqs. (7.1) and (7.2) follow the Model Code recommendations [39]. In which, E_{ci} and E_c are the modulus of elasticity and a reduced modulus of elasticity to account for initial plastic strain, respectively, given by $E_{ci} = 10{,}000(f_{cm})^{1/3}$ and $E_c = (0.8 + 0.2f_{cm}/88)E_{ci}$ [39]. ε_{cm} is strain corresponding to f_{cm}. In Eq. (7.4), $G_{ch} = (f_{cm}/f_{tm})^2 G_F$ is the crushing energy per unit area, l_{char} is the element characteristic length taken as the element volume divided by the largest face area for C3D8R elements, parameter b, the ratio of compressive plastic strain ε_c^{pl} to crushing strain ε_c^{ch}, can be initially assumed to be 0.9 and finally determined by iterative calculations.

In terms of tensile behaviour, the first part is defined as linearly elastic reaching $f_{t0} = f_{tm}$, as expressed by Eq. (8.1). The limit of linear tensile stress f_{t0} is equal to mean value of concrete axial tensile strength f_{tm}. The second part is defined as a function of tensile stress ratio σ_t/f_{tm} and crack width w, which was proposed in [40] and given by Eq. (8.2).

$$\sigma_{t(1)} = E_c \varepsilon_t \tag{8.1}$$

$$\frac{\sigma_{t(2)}}{f_{tm}} = \left[1 + \left(c_1\frac{w}{w_c}\right)^3\right] e^{-c_2\frac{w}{w_c}} - \frac{w}{w_c}\left(1 + c_1^3\right)e^{-c_2} \tag{8.2}$$

$$\varepsilon_t = \varepsilon_{tm} + w/l_{char} \tag{8.3}$$

In Eq. (8.2), $c_1 = 3.0$, $c_2 = 6.93$ [40]; $w_c = 5G_F/f_{tm}$ is the critical crack width and $G_F = 0.073f_{cm}^{0.18}$ is the fracture energy of concrete with unit N/mm proposed in [39]. Under the assumption that there is a single crack per element, the tensile strain ε_t can be acquired in terms of crack width from the kinematic relation of Eq. (8.3), where ε_{tm} is the tensile strain corresponding to f_{tm} and l_{char} is the element characteristic length.

The concrete compressive strength of cubic specimens was tested in [8] and mean value of the compressive strength $f_{cm,cube}$ at the concrete age of 28 days is 48.9 MPa. According to the function to describe the concrete strength with time proposed in [39], the mean value of $f_{cm,cube}$ at the average concrete age of 66 days of the push-out tests is 52.4 MPa, based on which mean value of concrete cylinder compressive strength is estimated to be 42.4 MPa. Table 3 lists the concrete properties used in determining the uniaxial stress-strain behaviours according to Eqs. (7) and (8).

Fig. 12 depicts the stress-strain curves for concrete under compression and tension according to Eqs. (7) and (8). Three element characteristic lengths 5, 20, and 50 mm are used to illustrate their effects on concrete softening behaviour both under compression and tension. Their effects on failure mode of push-out tests will be discussed in the following section. The ratio b of compressive plastic strain ε_c^{pl} to crushing strain ε_c^{ch} is 0.991, 0.946, and 0.870 after iterative calculations when characteristic length l_{char} equals 5, 20, and 50 mm, respectively. A larger l_{char} generates a smaller value for ratio b. It is clear that the compressive and tensile softening branches, expressed by Eqs. (7.3) and (8.2), are relevant to the characteristic length l_{char}. Using a smaller l_{char} would lead to a stiffer softening branch both in compressive and tensile uniaxial stress-strain curves.

4.3. *Concrete plasticity model*

For the plasticity model, yield condition is based on the loading function established in [41] with modifications proposed in [42] to account for tension and compression strength evolution. The yield condition has been incorporated into the concrete plasticity model in ABAQUS [26]. Only parameters K_c and f_{b0}/f_{c0} need to be input. K_c is the ratio of second stress invariants on tensile and compressive meridians. f_{b0} and f_{c0} are the biaxial and uniaxial compressive yield strengths.

The plasticity model assumes non-associated potential plastic flow. The flow potential uses the Drucker-Prager hyperbolic function, which is also adopted in concrete plastic model in ABAQUS. Two parameters, dilation angle ψ and eccentricity of the plastic potential surface ϵ, need to be input. Detailed explanations for concrete plasticity model can be found in [38] and the input values for dilation angle ψ, eccentricity ϵ, ratio of biaxial and uniaxial compressive yield strengths f_{b0}/f_{c0}, and the ratio of second stress invariants K_c, are 30°, 0.1, 1.16, 0.7 respectively, with reference to [38].

4.4. *Concrete damage variable*

The compressive and tensile damage variables d_c and d_t are defined as the portion of normalized energy dissipated by damage in the proposed approach [38], as expressed in Eq. (9).

$$d_c = \frac{1}{g_c}\int_0^{\varepsilon_c^{ch}} \sigma_c d\varepsilon_c^{ch} \tag{9.1}$$

$$d_t = \frac{1}{g_t}\int_0^{\varepsilon_t^{ck}} \sigma_t d\varepsilon_t^{ck} \tag{9.2}$$

In Eq. (9), ε_c^{ch} and ε_c^{ck} are the crushing strain and cracking strain, respectively; g_c and g_t denotes the energy per unit volume dissipated by damage in the whole damage process. Under the assumption that the relations of compressive stress vs. crushing strain and tensile stress vs. cracking strain can be described using exponential expression proposed by [41], the compressive and tensile damage functions are then derived as expressed by Eq. (10).

$$d_c = 1 - \frac{1}{2 + a_c}\left[2(1 + a_c)exp\left(-b_c\varepsilon_c^{ch}\right) - a_c exp\left(-2b_c\varepsilon_c^{ch}\right)\right] \tag{10.1}$$

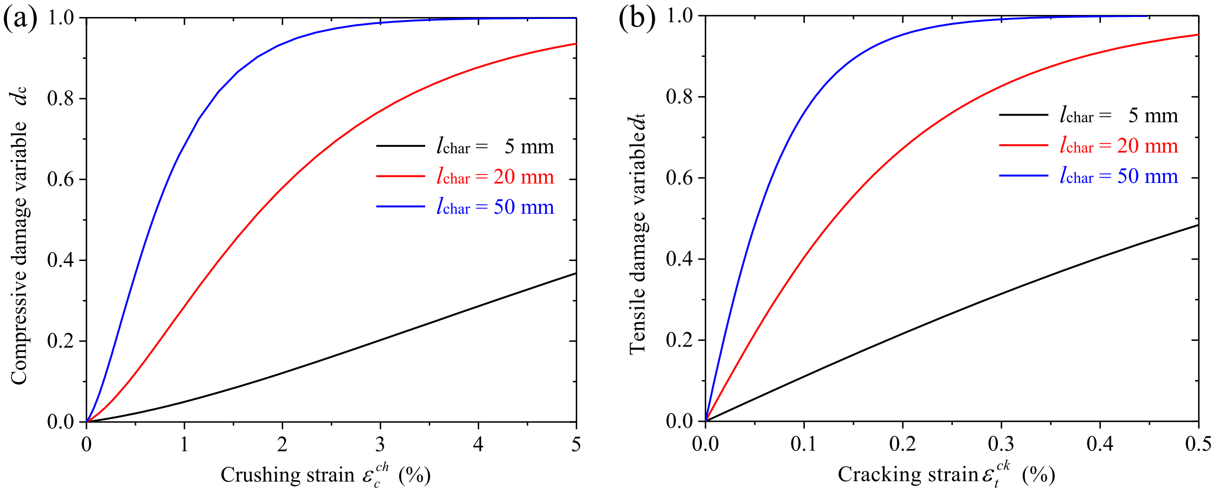

Fig. 13. Compressive and tensile damage variables.

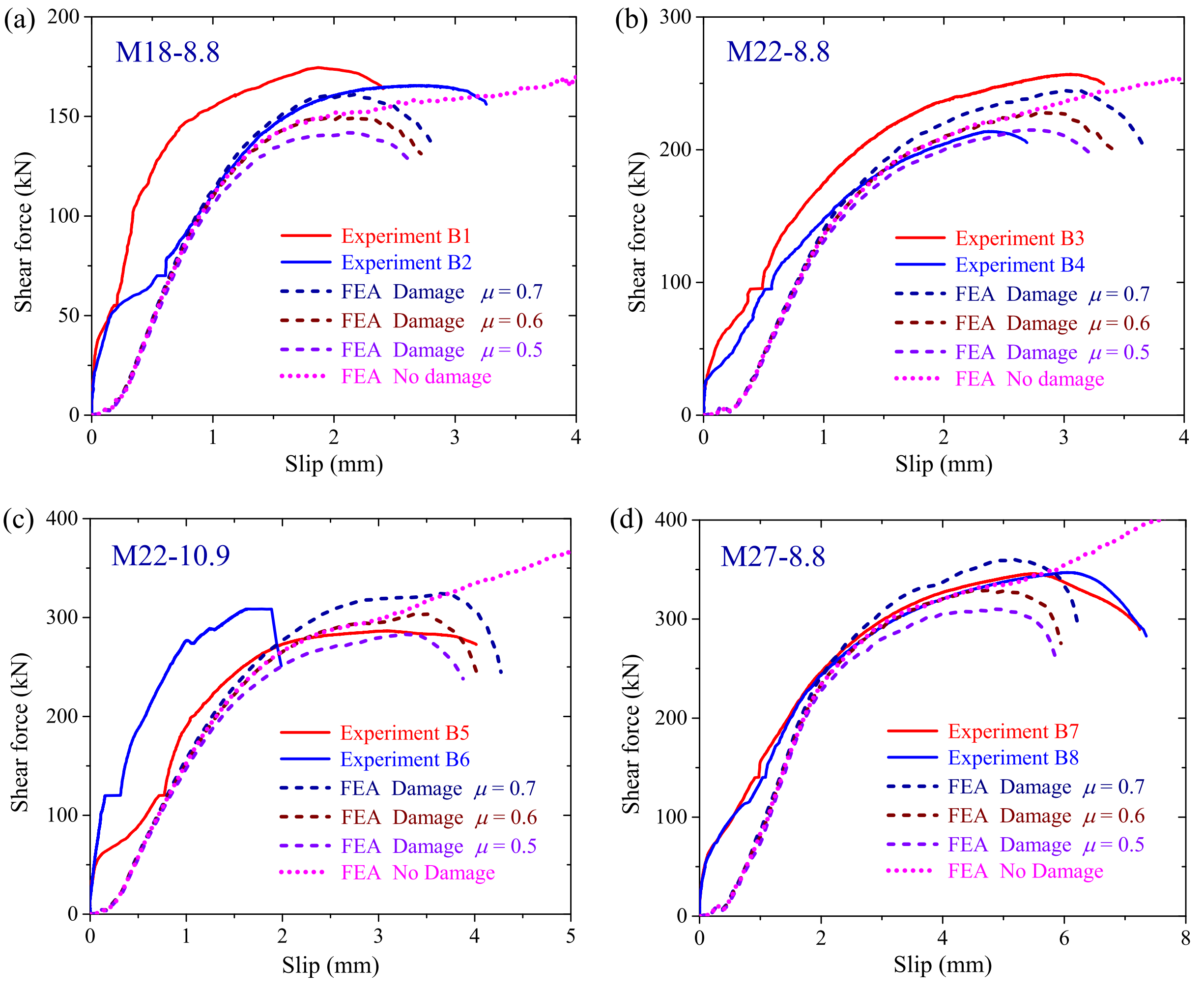

Fig. 14. Experimental and FEA load-slip curves of push-out tests.

Table 4
Comparisons of experimental and FEA shear resistance and corresponding slip ($\mu = 0.6$).

Specimen		Push-out shear resistance				Push-out slip at maximum load			
		Experiment (kN)	Mean (kN)	FEA (kN)	Ratio 1	Experiment (mm)	Mean (mm)	FEA (mm)	Ratio 2
M18-8.8	B1	174.5	170.1	150.8	0.89	1.87	2.28	2.07	0.91
	B2	165.6				2.68			
M22-8.8	B3	256.8	235.3	228.2	0.97	3.05	2.73	2.79	1.03
	B4	213.8				2.40			
M22-10.9	B5	286.6	297.7	303.5	1.02	3.09	2.36	3.37	1.43
	B6	308.7				1.63			
M27-8.8	B7	345.8	346.4	329.1	0.95	5.50	5.77	4.52	0.78
	B8	347.0				6.03			

$$d_t = 1 - \frac{1}{2 + a_t}\left[2(1 + a_t)exp\left(-b_t\varepsilon_t^{ck}\right) - a_t exp\left(-2b_t\varepsilon_t^{ck}\right)\right] \tag{10.2}$$

In Eq. (10), damage variable d_c is determined by crushing strain ε_c^{ch} with parameters a_c and b_c, while damage variable d_t is determined by cracking strain ε_c^{ck} with parameter a_t and b_t. Parameters a_c, a_t and b_c, b_t can be calculated using Eq. (11).

$$a_c = 2(f_{cm}/f_{c0}) - 1 + 2\sqrt{(f_{cm}/f_{c0})^2 - (f_{cm}/f_{c0})} \tag{11.1}$$

$$a_t = 2(f_{tm}/f_{t0}) - 1 + 2\sqrt{(f_{tm}/f_{t0})^2 - (f_{tm}/f_{t0})} \tag{11.2}$$

$$b_c = \frac{f_{c0}l_{char}}{G_{ch}}\left(1 + \frac{a_c}{2}\right) \tag{11.3}$$

$$b_t = \frac{f_{t0}l_{char}}{G_F}\left(1 + \frac{a_t}{2}\right) \tag{11.4}$$

In Eq. (11.1), $f_{c0} = 0.4f_{cm}$ is the limit of linear compressive stress, producing $a_c = 7.783$; $f_{t0} = f_{tm}$ is the limit of linear tensile stress, producing $a_t = 1.0$; b_c and b_t are relevant to the element characteristic length l_{char}.

Fig. 13 exhibits the relations of compressive damage variable vs. crushing strain and tensile damage variable vs. cracking strain. Three element characteristic lengths 5, 20, and 50 mm are used to calculate and compare the damage variables. At the same crushing strain or cracking strain, the compressive and tensile damage variables have much larger values if a bigger l_{char} is used in calculations. In the following analysis, the concrete element characteristic length l_{char} is set to 5 mm at first, same as the concrete mesh size around the bolted connector, to model the concrete behaviors in push-out tests. Then, much larger l_{char} equal to 20 and 50 mm for the identical mesh size around 5 mm are used to investigate the effects of less stiff concrete softening behaviors on the failure mode of push-out tests.

5. FEA results of push-out tests

5.1. Load-slip curves

Push-out models for M18-8.8, M22-8.8, M22-10.9, and M27-8.8 specimens are established and Fig. 11 shows the model of M22 specimen with each component. In FE simulations, the clearance for M18, M22, and M27 bolt hole are set to 0.2, 0.3, and 0.5 mm, respectively, with reference to the measured clearances in experimental tests [8]. Therefore, the hole diameter for push-out models with M18, M22, and M27 bolts are 18.02, 22.03, and 27.05 mm, respectively. The yield and ultimate strengths of steel plate, shown in Fig. 11b, are 390 MPa and 535 MPa, and bilinear true stress-strain curve is used for the steel plate with true yield stress equal to 390 MPa and true "ultimate strength" equal to 640 MPa at true strain 0.2. Only the elastic properties are considered for the steel rebars, which are shown in Fig. 11c, since the steel rebars have very low stress in the push-out specimens. Same elasticity and plasticity behaviors are considered for short bolt, coupler, and long bolt in a push-out model. Concrete behaviors corresponding to element characteristic length $l_{char} = 5$ mm are considered in each model, as the concrete mesh size around the bolted connector is about 5 mm, where the concrete would experience large plastic deformations. The push-out models are calculated using the explicit solver in ABAQUS. The target time increment is set to 0.002 s and the duration of the push-out step is 200 s.

General contact is used to simulate all the contacts in the push-out model, including the contact between bolted connector and concrete, steel plate and concrete, steel plate and bolt, concrete and base, and the contact in the engagement region of bolt and coupler. The normal behaviour of the general contact is modelled using "hard" contact, while the tangential behaviour is modelled using "penalty" friction formulation with a friction coefficient μ. Although the friction coefficient in the steel-steel contact surface may be different from that in the steel-concrete contact surface, a unified friction coefficient μ is used for the whole model to reduce the computational cost. According to experimental investigations in [43], the friction coefficient μ at the steel-concrete interface would be over 0.5. In the simulations of push-out tests, the friction coefficient μ is set to 0.5, 0.6, and 0.7 to check its effects on the shear performance of each bolted connector in push-out tests.

Fig. 14 shows the experimental and numerical load-slip curves of four groups of push-out tests M18-8.8, M22-8.8, M22-10.9, and M27-8.8, in which the experimental curves have been reported in [8]. In the numerical analysis, the BW criterion of Eq. (5) with $C_1 = 0.5$ and $C_2 = 1.4$ are considered in the material behaviour of short bolts. Three calculations with friction coefficient $\mu = 0.5, 0.6, 0.7$ are performed for each group of push-out test. In the actual push-out tests, there exists cohesive force at the steel-concrete interface when the push-out load is relatively small. However, in the numerical analyses, only the friction force at the steel-concrete interface is considered through defining a friction coefficient μ in the general contact. Consequently, the slip at the steel-concrete interface for each push-out specimen in the numerical analyses is relatively larger than in the actual experimental tests when the push-out load is relatively small, which can be seen in Fig. 14. Except for B1 and B6 specimens, the numerical load-slip curves of other push-out specimens would be close to their experimental curves when the slip at the steel-concrete interface is larger than 1 mm, as the cohesion at the steel-concrete interface would not contribute to the shear capacity of each push-out specimen.

It can be concluded from Fig. 14 that the shear resistance for each group of push-out tests could be approximately estimated if an appropriate friction coefficient is considered. For M18-8.8 push-out tests, using $\mu = 0.7$ would predict the push-out shear resistance better than using smaller friction coefficients. For other three groups of push-out tests, their shear resistances could be better estimated using $\mu = 0.6$. The slip at the maximum load could also be approximately estimated using the BW criterion. If the fracture criterion is not incorporated in the modelling, the shear force in the modelling of push-out tests would

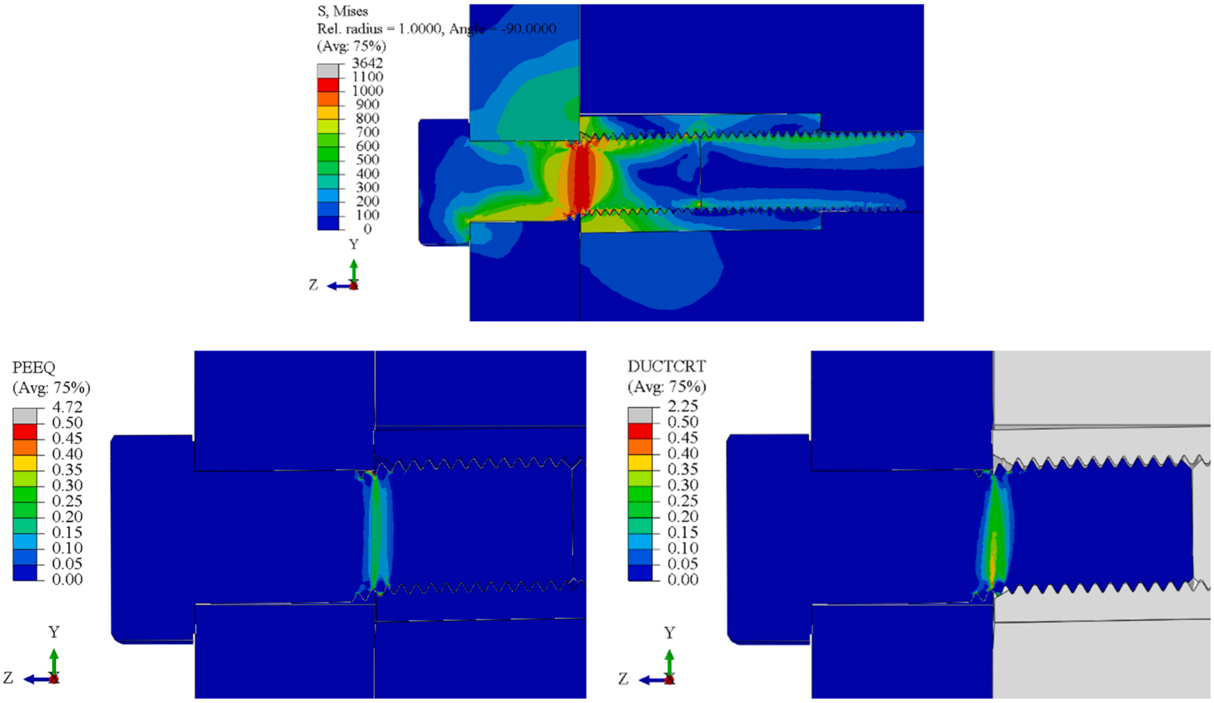

Fig. 15. Contour plots of Mises stress, PEEQ, DUCTCRT for M22-8.8 at its maximum load.

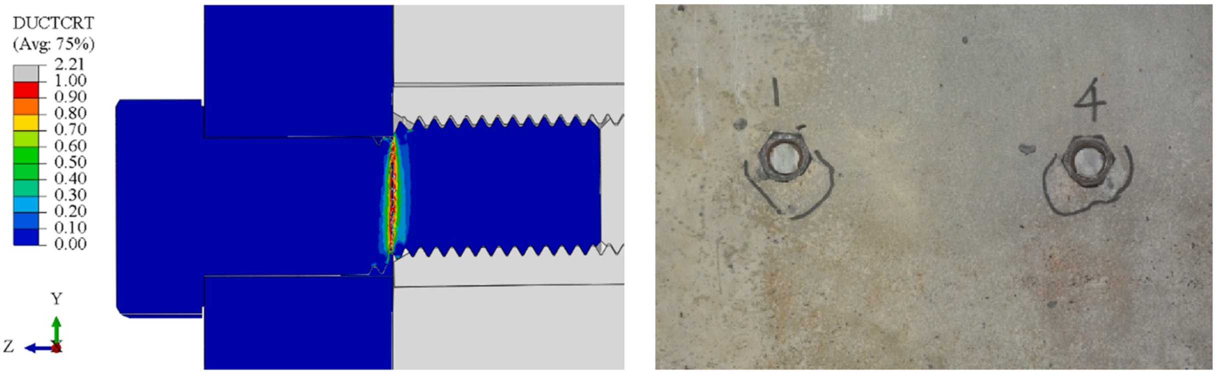

Fig. 16. Contour plot of DUCTCRT and failure model of M22-8.8 after fracture.

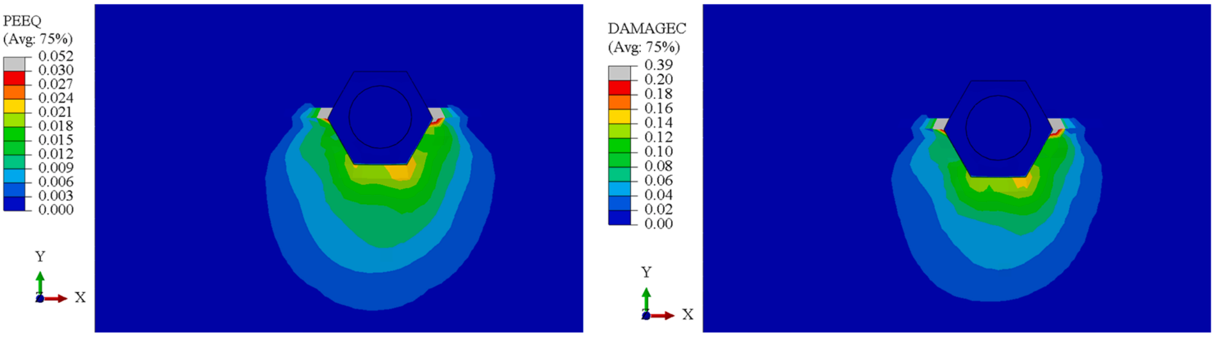

Fig. 17. Contour plots of PEEQ, damage variable of concrete for M22-8.8.

present a continuously increasing trend and the shear resistance and the deformation capacity of the “bolt-coupler” connectors would be overestimated, see the curves without considering damage model in Fig. 14.

Table 4 lists the experimental and numerical shear resistances and the corresponding slips for each group of push-out tests. Although there are some gaps for the deformation capacity of M18-8.8 and M22-10.9 push-out tests and for the shear resistance of M22-8.8 push-out tests between the numerical and experimental results. The mean values of shear resistance and corresponding slip for two tests of each group are compared with the corresponding FEA results under $\mu = 0.6$. Ratio 1 in

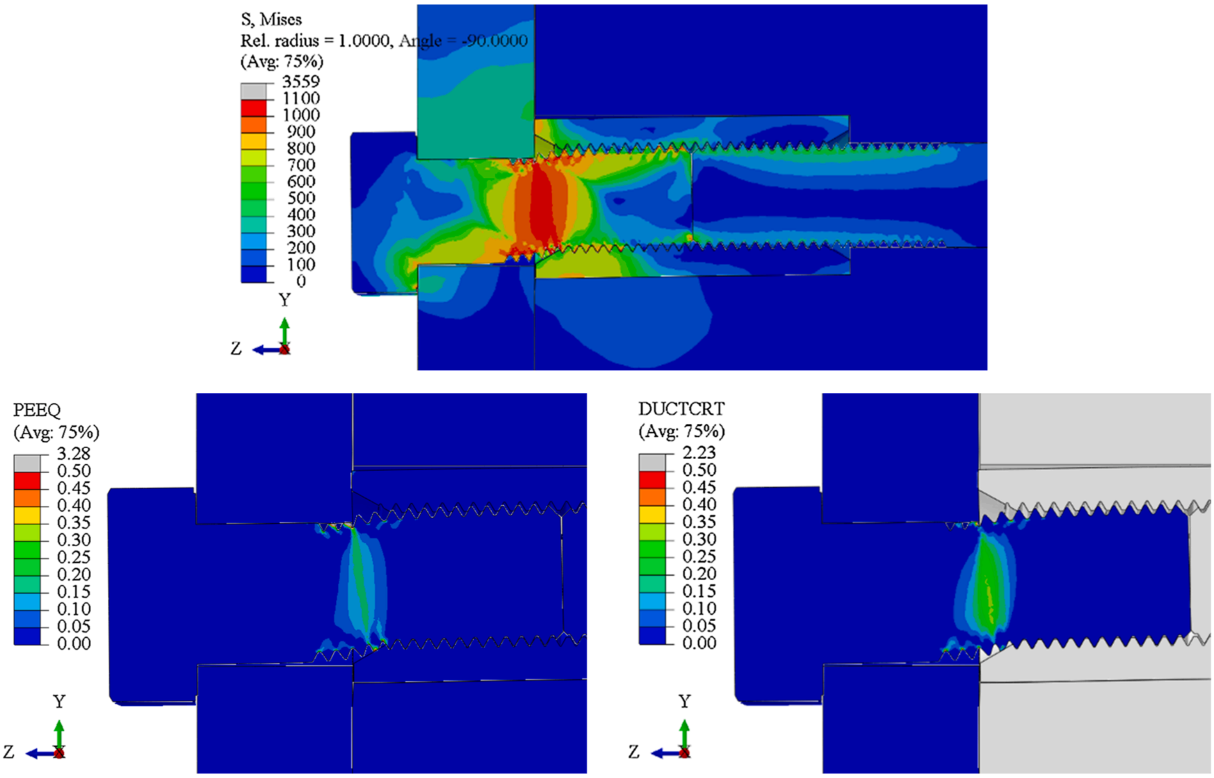

Fig. 18. Contour plots of Mises stress, PEEQ, DUCTCRT for M27-8.8 at its maximum load.

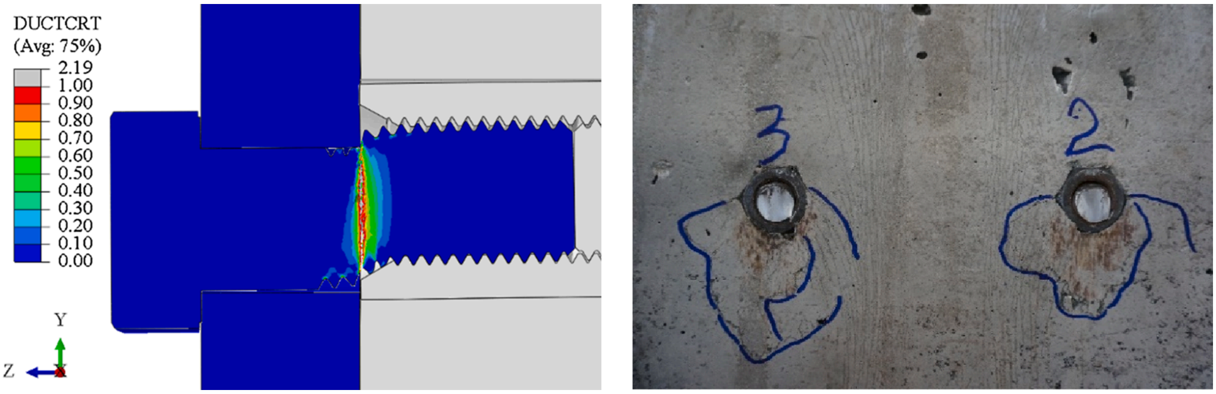

Fig. 19. Contour plot of DUCTCRT and failure mode of M27-8.8 after bolt fracture.

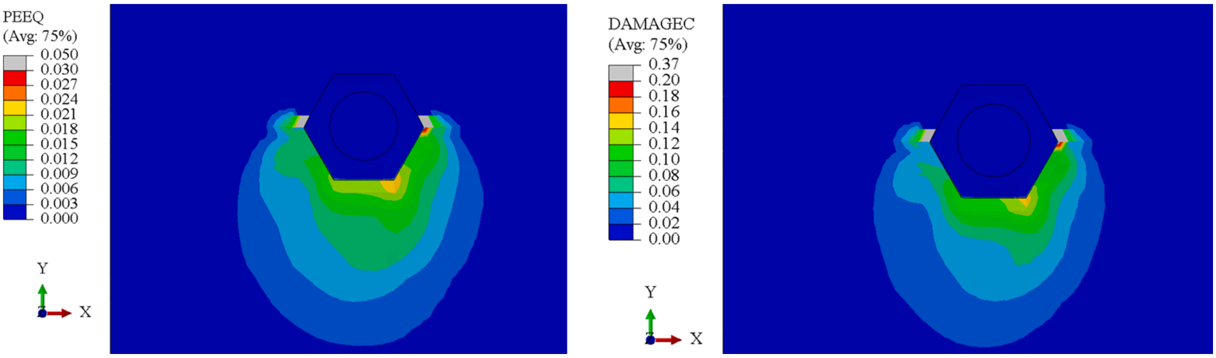

Fig. 20. Contour plots of PEEQ, damage variable of concrete for M27-8.8.

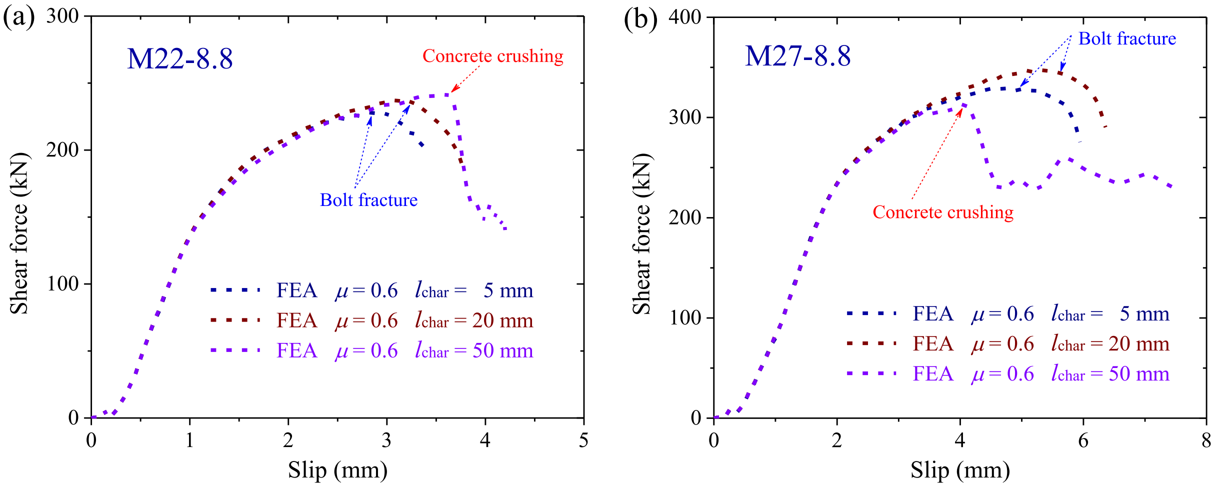

Fig. 21. Load-slip curves for M22-8.8 and M27-8.8 with different concrete behaviours.

Table 4 stands for the ratio of the numerical shear resistance to the mean value of the experimental shear resistance for each group of bolted connectors. Ratio 2 denotes the ratio of the numerical slip at the maximum load to the corresponding experimental value. Values of Ratio 1 listed in Table 4 indicate that the shear resistance of M22 and M27 push-out tests can be accurately estimated but that of M18 push-out test is underestimated by 11%. Values of Ratio 2 indicate that the slip at maximum load, representing the deformation capacity of the bolt-coupler connectors, can be approximately estimated for push-out tests if specimen B6 is excluded.

5.2. *Stress, strain and failure modes*

The stress, strain and failure mode of M22-8.8 and M27-8.8 push-out specimens are presented in this section to illustrate the detailed behaviour of the bolt-coupler connectors. Fig. 15 shows the contour plots of Mises stress, PEEQ, and damage index (DUCTCRT) for M22-8.8 at maximum load of the push-out test. The maximum Mises stress in the shear plane of M22-8.8 is about 1100 MPa, which is close to the Mises stress when M22-8.8 bolt gets to its maximum load under pure shear state as shown in Fig. 8. PEEQ and damage index locate in the region near the shear plane, the maximum damage index in the shear plane is less than 0.4, and the corresponding maximum PEEQ is around 0.2.

When damage index of the short bolt in its shear plane gets to 1.0 in the simulation, the fracture would suddenly occur with a brittle failure mode as observed in experiments. Fig. 16 exhibits the numerical and experimental fracture mode of the short bolt. A smooth fracture plane almost perpendicular to bolt axis can be observed. Fig. 17 shows the contour plots of PEEQ and compressive damage variable of concrete for M22-8.8 specimen. The concrete maximum PEEQ beneath the coupler is about 0.02 in a small region, indicating that concrete in this small region occurs a little softening behaviour and the maximum compressive damage variable in this region is less than 0.16.

Fig. 18 shows the contours plots of Mises stress, PEEQ, and damage index for M27-8.8 at maximum load of the push-out test. The maximum Mises stress in the shear plane of M27-8.8 bolt is also about 1100 MPa same as the maximum Mises stress of M22-8.8 bolt, since these two bolts have almost the same stress-strain behaviour as shown in Fig. 2. The maximum PEEQ and damage index in the shear plane of M27-8.8 bolt at the maximum load are about 0.2 and 0.4, respectively. Fig. 19 shows the numerical and experimental failure mode of the short bolt M27. Significant shear deformation of M27 bolt near the shear plane can be observed, which leads to a larger slip corresponding to the shear resistance. Fig. 20 exhibits the contour plots of PEEQ and compressive damage variable of concrete for M27-8.8 specimen. Almost identical maximum PEEQ and compressive damage variable can be observed beneath the coupler compared to those in M22-8.8 specimen shown in Fig. 17.

5.3. *Effect of concrete softening behaviour*

The above numerical results are based on concrete behaviour with characteristic length $l_{char} = 5$ mm, which is close to the concrete mesh size around the bolt-coupler connector. Bolt fracture in each push-out model is numerically acquired without concrete crushing. To check the effect of concrete softening behaviour on the numerical results, concrete behaviours with $l_{char} = 20$ and 50 mm, as shown in Figs. 12 and 13, are input in M22-8.8 and M27-8.8 push-out models.

Fig. 21 shows the load-slip curves for M22-8.8 and M27-8.8 specimens with friction coefficient equal to 0.6 and $l_{char} = 5$, 20, 50 mm. If $l_{char} = 20$ mm is used, the shear resistance and corresponding slip would slightly increase compared with using the actual $l_{char} = 5$ mm. Under

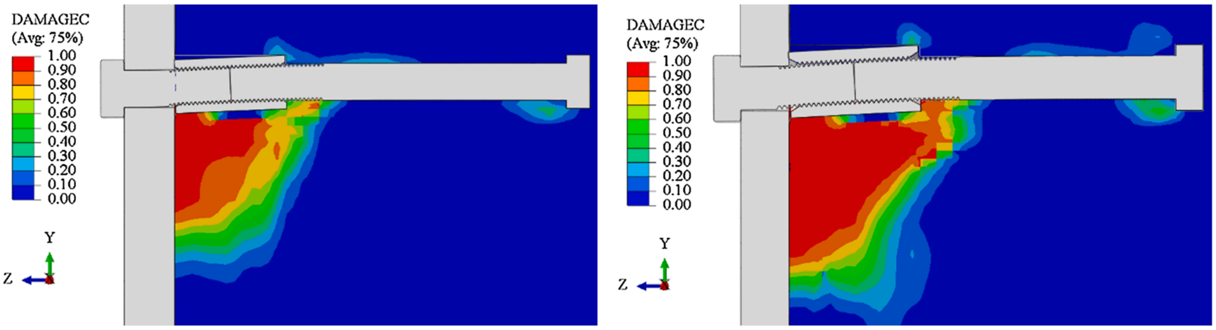

Fig. 22. Contour plots of compressive damage variables for M22-8.8 and M27-8.8 with $l_{char} = 50$.

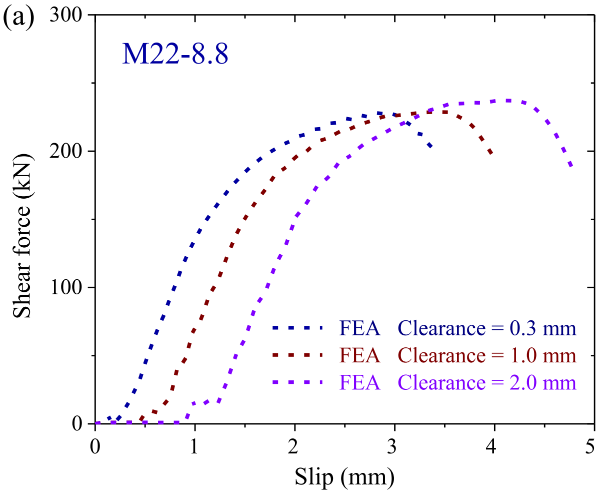

Fig. 23. Load-slip curves of M22-8.8 and M27-8.8 with various clearances.

these two cases, their failure modes are governed by bolt fracture. If l_{char} = 50 mm is used to determine the concrete stress–strain constitutive relationship in the descending portion, the actual characteristic element length l_{char} = 5 mm, the softening branches under compression are significantly underestimated as shown in Fig. 13. Consequently, the failure modes of the push-out tests using concrete stress-strain constitutive relationship with l_{char} = 50 mm is the concrete crushing instead of bolt shear fracture. It can be seen from Fig. 21a that using concrete stress-strain constitutive relationship with l_{char} = 50 mm would lead to the maximum shear resistance with concrete crushing failure mode. This is because the less stiff concrete in the softening stage before the final crushing would increase the maximum friction force at the steel-concrete interface. The shear resistance corresponding to l_{char} = 20 mm is also slightly larger than that corresponding to l_{char} = 5 mm both for M22-8.8 and M27-8.8 push-out tests. For M27-8.8 push-out test, using concrete stress-strain constitutive relationship with l_{char} = 50 mm would lead to concrete crushing failure with a reduced shear resistance.

Fig. 22 exhibits the contour plots of compressive damage variables for M22-8.8 and M27-8.8 models with l_{char} = 50 mm after the concrete crushing. The concrete beneath the coupler will crush when the push-out load approaches the shear resistance. Therefore, the concrete softening branches should be carefully considered and the adopted mesh-dependent concrete uniaxial stress-strain curves are reasonable for the calculations.

5.4. Effect of clearance in bolt hole

In above simulations, very small clearances in bolt holes, 0.3 mm for M22 bolt and 0.5 mm for M27 bolt, were considered same as in the actual experiments. The nominal clearances specified in EN 1090-2 [44] are 2 mm for M22 bolts and 3 mm for M27 bolts. Therefore, two clearances 1 and 2 mm for M22-8.8 bolt and 1.5 and 3 mm for M27 bolt are modelled to check their effects on the shear performance of the bolt-coupler connectors. Fig. 23 shows the load-slip curves of M22-8.8 and M27-8.8 specimens with three clearances. The increase of clearance in bolt hole for these two groups of push-out specimens makes the initial slip at the beginning of loading more apparent. The shear stiffness with different hole clearances for these two groups of push-out models is almost identical in the loading stage. This indicates that the clearance in bolt hole only affect the initial slip and has little effects on the bolt shear stiffness and shear resistance.

5.5. Effect of pretension

In practical application of the bolt-coupler connectors, the short bolts in bolted connectors could be tightened to raise the initial shear stiffness. The nominal clearances specified in EN 1090-2 [44] are adopted to analyse the effect of pretension on the shear performance of the bolt-coupler connectors. To simulate the tightening process of short bolts, a rotation angle is applied on the short bolt head in the first analysing step. The rotation angle of short bolts is relevant to the bolt pretension specified, the friction coefficient between bolt and coupler, the bolt diameter and so on. Therefore, for a push-out specimen, the short bolt pretension vs. the rotation angle relationship can be obtained through applying a much larger rotation angle on the short bolt head in the numerical analysis. The pretension of short bolt is equal to the contact

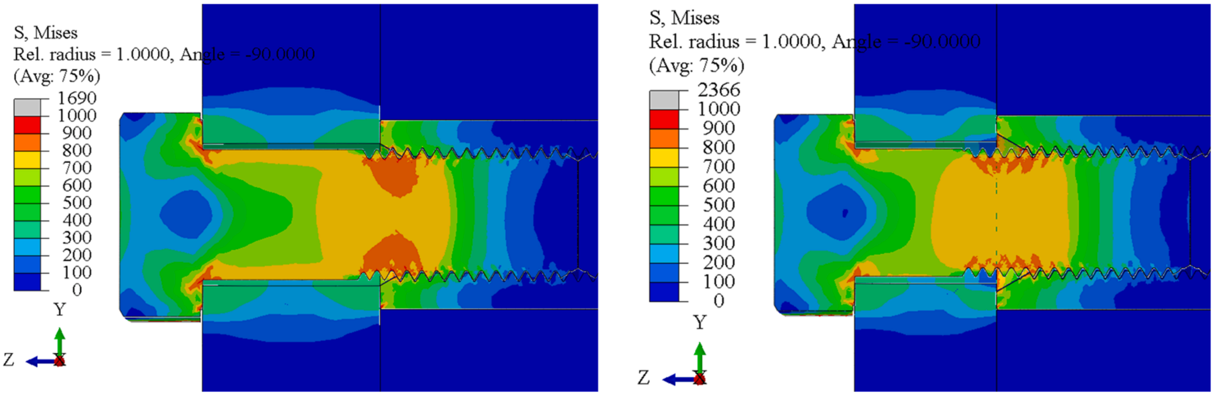

Fig. 24. Contour plots of Mises stress after pretension of bolts (left, M22; right, M27).

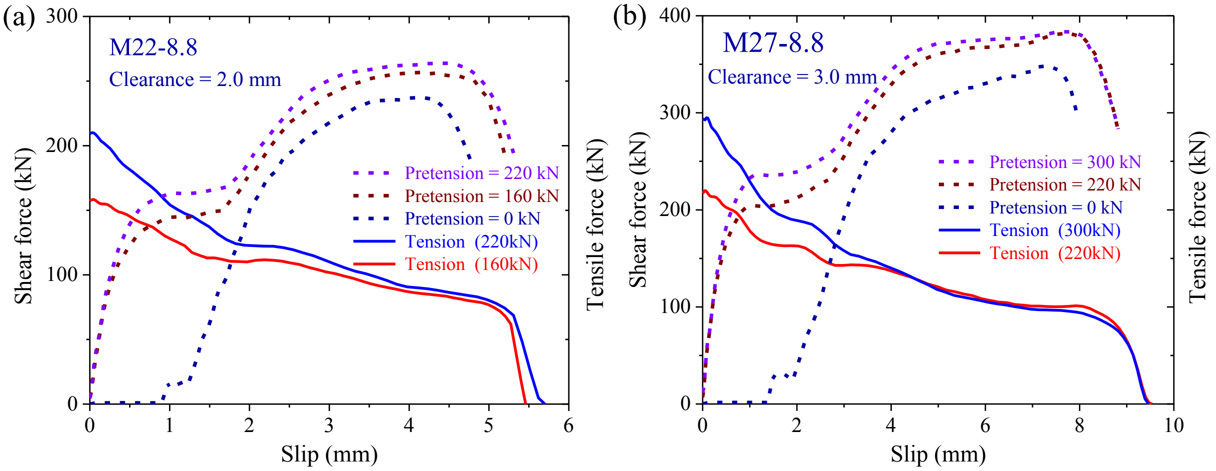

Fig. 25. Variation of bolt tension and load-slip curves with and without pretension.

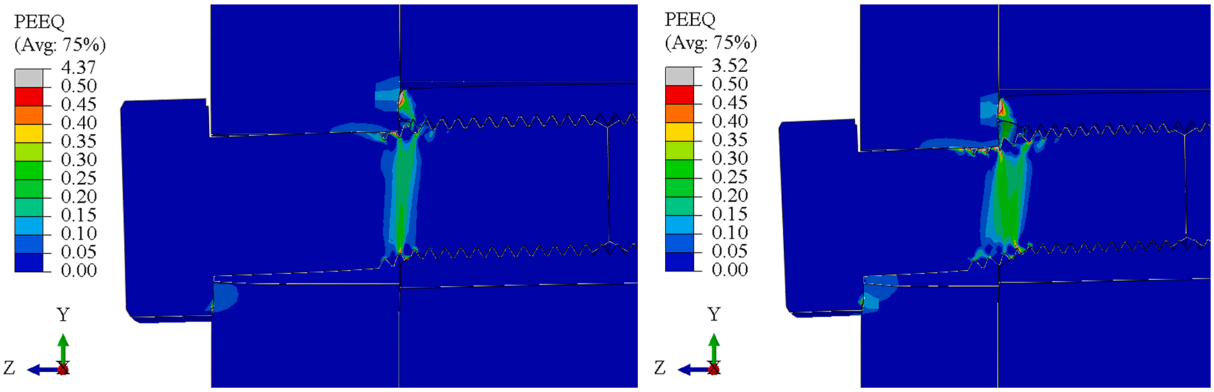

Fig. 26. Contour plots of PEEQ at maximum loads for M22-8.8 and M27-8.8.

pressure between short bolt and steel plate, which can be output from the push-out specimen corresponding to each rotation angle applied on the short bolt head. Then a specified short bolt pretension can be realized in the "turn-of-bolt" loading step through applying a corresponding rotation angle for the short bolt in the push-out specimen.

In the simulation of non-preloaded push-out tests, the friction coefficient in the general contact is set to 0.6 for modelling all the surface friction properties. However, for simulating the tightening process of the preloaded push-out tests, if the friction coefficient equal to 0.6 is considered for the friction properties of the contacting surfaces between short bolt and coupler, the threaded portion of the short bolt would be very difficult to be screwed into the coupler due to the much larger friction coefficient, and the shank of the short bolt would occur significant torsion deformation apart from the uniaxial extension. To reduce the shank torsion deformation of the short bolt in the "turn-of-bolt" loading step, a more rational friction coefficient $\mu = 0.1$ is used instead of $\mu = 0.6$ to allow for the pretension of short bolt to be realized.

Two pretensions of 160 and 220 kN are applied on M22-8.8 bolts, which are 55% and 75% of the tensile resistance 290 kN of M22-8.8 bolts. Two pretensions of 220 and 300 kN are applied on M27-8.8 bolts, which are near 50% and 70% of the tensile resistance 436 kN of M27-8.8 bolts. Fig. 24 shows the contour plots of Mises stress after applying pretension 220 and 300 kN for M22-8.8 and M27-8.8 bolts, respectively. The maximum Mises stress occurs in the threaded region of short bolt near the shear plane. For M22 and M27 bolts, their maximum Mises stresses are as large as 1000 MPa, larger than their yield strengths, indicating that the bolts have entered the plastic stage after the larger pretension. Besides, it can be seen from Fig. 24 that the pretension of short bolt would make the short bolt, steel plate, and coupler to be an integrated shear load transferring connector. When the shear load is less than the friction force between steel plate and coupler, the shear load will be transferred from the steel plate to the concrete beneath the coupler through the coupler.

Fig. 25 shows the variation of bolt tension and load-slip curves with and without pretension. The applied pretension in bolts in the first loading step would decrease gradually in the second loading step with the increase of the push-out displacement in both groups of push-out models. In terms of the load-slip curves of push-out specimens with pretensions, there are four stages including the initial linear stage, the slipping stage due to the clearance, the nonlinear increasing stage, and the final descending stage. Clearly, applying pretension in short bolts delays the bolt slipping in holes from initial loading to the state that the push-out load exceeds the friction force at the steel-concrete interface. Applying pretension in short bolts would slightly increase the shear resistance of bolted connectors in push-out tests. The deformation capacity of bolts at the ultimate state is hardly affected by applying pretension.

Fig. 26 exhibits the contour plots of PEEQ at maximum loads for M22-8.8 and M27-8.8 models with 220 kN and 300 kN pretension, respectively. Significant plastic strain can be observed at the top region of the coupler. The friction force due to the contact between the top region of the coupler and the adjacent steel plate contributes part of shear force for the push-out specimen. The maximum PEEQs at the shear plane of M22-8.8 and M27-8.8 bolts are not larger than 0.3 for most regions.

6. Conclusion

Fracture simulations of push-out tests on a demountable bolted connector are performed in this paper. Tensile loadings and pure shear loadings on four groups of bolts are modelled to calibrate the bolt stress-strain behaviour and the fracture criterion. For modelling the push-out tests, a concrete damage model relevant to element characteristic length is used. The effects of friction coefficient, concrete softening behaviour, hole clearance, pretension on the shear performance of push-out specimens are discussed. Conclusions can be drawn as follows.

(1) The tensile resistance of bolts F_t can be estimated as $0.97 f_u A_s$, f_u and A_s are the ultimate strength of the bolt material and tensile stress area of the bolt. The pure shear resistance of bolts F_v can be estimated as $0.6F_t$, same as the specification in Eurocode.
(2) The friction force at the steel-concrete interface contributes a part of the shear resistance in push-out tests. The friction coefficient at the steel-concrete interface is as large as 0.6, with which the experimental load-slip curves can be well-estimated by the numerical analysis.
(3) The deformation capacity of bolts in push-out tests can be well-estimated by using the BW fracture criterion in the analyses with $C_1 = 0.5$ and $C_2 = 1.4$. For bolts under pure shear state, its fracture equivalent plastic strain (PEEQ) is about 0.5, governed by parameter C_1 in the BW fracture criterion.
(4) The softening branches of concrete uniaxial behaviour need to be carefully determined in the numerical analysis of push-out tests. The used mesh-dependent softening branches are effective and accurate, with which the fracture of bolts is numerically acquired rather than that the concrete crushing governs the final failure mode of push-out tests.

CRediT authorship contribution statement

Fei Yang: Visualization, Methodology, Investigation, Validation, Formal analysis, Writing - original draft. **Yuqing Liu:** Conceptualization, Supervision, Writing - review & editing. **Haohui Xin:** Supervision, Writing - review & editing. **Milan Veljkovic:** Supervision, Writing - review & editing.

Declaration of Competing Interest

The authors declare that they have no known competing financial interests or personal relationships that could have appeared to influence the work reported in this paper.

Acknowledgements

The first author would like to acknowledge the financial support provided by the China Scholarship Council (CSC) [Grant number: 201806260196].

References

[1] Dai X, Lam D, Saveri E. Effect of concrete strength and stud collar size to shear capacity of demountable shear connectors. J Struct Eng 2015;141(11):04015025.
[2] Lam D, Dai X, Ashour A, Rahman N. Recent research on composite beams with demountable shear connectors. Steel Constr 2017;10(2):125–34.
[3] Rehman N, Lam D, Dai X, Ashour A. Testing of composite beam with demountable shear connectors. Proc Inst Civ Eng – Struct Build 2018;171(1):3-16.
[4] Sencu RM, Wang Y, Yang J, Lam D. Performance evaluation of demountable shear connectors with collar step at ambient and elevated temperatures. Eng Struct 2019;194:94–105.
[5] Kwon G, Engelhardt MD, Klingner RE. Behavior of post-installed shear connectors under static and fatigue loading. J Constr Steel Res 2010;66(4):532–41.
[6] Kwon G, Engelhardt MD, Klingner RE. Experimental behavior of bridge beams retrofitted with postinstalled shear connectors. J Bridge Eng 2011;16(4):536–45.
[7] Azad ARG, Kreitman K, Engelhardt M, Helwig T, Williamson E. Large-scale fatigue testing of post-installed shear connectors in partially-composite bridge girders. J Constr Steel Res 2019;161:57–69.
[8] Yang F, Liu Y, Jiang Z, Xin H. Shear performance of a novel demountable steel-concrete bolted connector under static push-out tests. Eng Struct 2018;160:133–46.
[9] Yang F, Liu Y. Behavior of an innovative demountable steel-concrete connector under static loading. In maintenance, safety, risk, management and life-cycle performance of bridges: proceedings of the ninth international conference on bridge maintenance, safety and management (IABMAS 2018) Melbourne, Australia.
[10] Kozma A, Odenbreit C, Braun MV, Veljkovic M, Nijgh MP. Push-out tests on demountable shear connectors of steel-concrete composite structures. Structures 2019;21:45–54.
[11] Nijgh MP, Gîrbacea IA, Veljkovic M. Elastic behaviour of a tapered steel-concrete composite beam optimized for reuse. Eng Struct 2019;183:366–74.
[12] Nijgh MP, Veljkovic M. Requirements for oversized holes for reusable steel-concrete composite floor systems. Structures 2020;24:489–98.
[13] Wen H, Mahmoud H. Simulation of block shear fracture in bolted connections. J Constr Steel Res 2017;134:1–16.
[14] Feldmann M, Schaffrath S. Assessing the net section resistance and ductility requirements of EN 1993-1-1 and EN 1993-1-12. Steel Constr 2017;10:354–64.
[15] Feldmann M, Schaffrath S. Application of damage theory to structures made from high-strength steels. Steel Constr 2018;11:257–63.
[16] Xin H, Veljkovic M. Evaluation of high strength steels fracture based on uniaxial stress-strain curves. Eng Fail Anal 2021;120:105025.
[17] Song Y, Wang J, Uy B, Li D. Experimental behaviour and fracture prediction of austenitic stainless steel bolts under combined tension and shear. J Constr Steel Res 2020;166:105916.
[18] Song Y, Wang J, Uy B, Li D. Stainless steel bolts subjected to combined tension and shear: behaviour and design. J Constr Steel Res 2020;170:106122.
[19] Li D, Uy B, Wang J, et al. Behaviour and design of Grade 10.9 high-strength bolts under combined actions. Steel Compos Struct 2020;35(3):327–41.
[20] Li D, Uy B, Wang J, et al. Behaviour and design of high-strength Grade 12.9 bolts under combined tension and shear. J Constr Steel Res 2020;174:106305.
[21] Grimsmo EL, Aalberg A, Langseth M, Clausen AH. Failure modes of bolt and nut assemblies under tensile loading. J Constr Steel Res 2016;126:15–25.
[22] Yang F, Veljkovic M, Liu Y. Fracture simulation of partially threaded bolts under tensile loading. Eng Struct 2021;226:111373.
[23] EN ISO 898-1:2013 - Mechanical properties of fasteners made of carbon steel and alloy steel- Part 1: Bolts, screws and studs with specified property classes - Coarse thread and fine pitch thread, European Committee for Standardization, Brussels, Belgium.
[24] International Organization for Standardization (ISO), ISO 4014, Hexagon Head Bolts - Product Grades A and B, ISO, Switzerland; 2011.
[25] International Organization for Standardization (ISO), ISO 4032, Hexagon Regular Nuts (Style 1) – Product Grades A and B, ISO, Switzerland; 2012.
[26] Abaqus Analysis User's Guide, Version 6.13. Dassault Systèmes Simulia Corp., Providence, RI, USA; 2013.
[27] Pavlovic M, Markovic Z, Veljkovic M, et al. Bolted shear connectors vs. headed studs behaviour in push-out tests. J Constr Steel Res 2013;88:134–49.
[28] Kodur V, Yahyai M, Rezaeian A, et al. Residual mechanical properties of high strength steel bolts subjected to heating-cooling cycle. J Constr Steel Res 2017;131:122–31.
[29] Yahyai M, Kodur V, Rezaeian A. Residual mechanical properties of high-strength steel bolts after exposure to elevated temperature. J Mater Civ Eng 2018;30(10):04018240.
[30] Yang F, Veljkovic M. Damage model calibration for S275 and S690 steels. ce/papers 2019;3(5–6):262–71.
[31] Yang F, Veljkovic M, Liu Y. Ductile damage model calibration for high-strength structural steels. Constr Build Mater 2020;263:120632.
[32] EN 1993-1-8, Design of steel structures, Part 1-8: Design of joints, European Committee for Standardization, Brussels, Belgium; 2005.
[33] Wierzbicki T, Bao Y, Lee YW, Bai Y. Calibration and evaluation of seven fracture models. Int J Mech Sci 2005;47(4–5):719–43.
[34] Noell PJ, Carroll JD, Boyce BL. The mechanisms of ductile rupture. Acta Mater 2018;161:83–98.
[35] Bao Y, Wierzbicki T. On fracture locus in the equivalent strain and stress triaxiality space. Int J Mech Sci 2004;46(1):81–98.
[36] Bao Y, Wierzbicki T. On the cut-off value of negative triaxiality for fracture. Eng Fract Mech 2005;72(7):1049–69.
[37] Renner A, Lange J. Load-bearing behaviour of high-strength bolts in combined tension and shear. Steel Constr 2012;5(3):151–7.
[38] Alfarah B, López-Almansa F, Oller S. New methodology for calculating damage variables evolution in Plastic Damage Model for RC structures. Eng Struct 2017;132:70–86.
[39] CEB-FIP. Model Code 2010 London: Thomas Telford; 2010.
[40] Hordijk DA. Tensile and tensile fatigue behaviour of concrete; experiments, modelling and analyses. Heron 1992;37(1):1–79.
[41] Lubliner J, Oliver J, Oller S, Oñate E. A plastic-damage model for concrete. Int J Solids Struct 1989;25(3):299–326.

[42] Lee J, Fenves GL. Plastic-damage model for cyclic loading of concrete structures. J Eng Mech 1998;124(8):892–900.

[43] Lee YH, Joo YT, Lee T, Ha DH. Mechanical properties of constitutive parameters in steel–concrete interface. Eng Struct 2011;33(4):1277–90.

[44] EN 1090-2: 2018 Execution of steel structures and aluminium structures - Part 2: technical requirements for steel structures, European Committee for Standardization, Brussels, Belgium.